NeuroImage 270 (2023) 119950

Contents lists available at ScienceDirect

NeuroImage

journal homepage: www.elsevier.com/locate/neuroimage

Age-related differences of cerebellar cortex and nuclei: MRI findings in healthy controls and its application to spinocerebellar ataxia (SCA6) patients ☆

Dominik Jäschke[a,b], Katharina M. Steiner[a,c], Dae-In Chang[a,d], Jens Claaßen[a,e], Ellen Uslar[a], Andreas Thieme[a], Marcus Gerwig[a], Viktor Pfaffenrot[f], Thomas Hulst[a,g], Alexander Gussew[h], Stefan Maderwald[f], Sophia L. Göricke[i], Martina Minnerop[j,k,l], Mark E. Ladd[f,m,n], Jürgen R. Reichenbach[o], Dagmar Timmann[a,f], Andreas Deistung[a,h,o,*]

[a] *Department of Neurology and Center for Translational Neuro- and Behavioral Sciences (C-TNBS), Essen University Hospital, University of Duisburg-Essen, Essen 45147, Germany*
[b] *Department of Radiology and Nuclear Medicine, University Hospital Basel, Basel 4031, Switzerland*
[c] *LVR-Hospital Essen, Department of Psychiatry and Psychotherapy, Medical Faculty, University of Duisburg-Essen, Essen 45147, Germany*
[d] *Clinic for Psychiatry, Psychotherapy and Preventive Medicine, LWL-University Hospital of the Ruhr-University Bochum, Bochum 44791, Germany*
[e] *Fachklinik für Neurologie, MEDICLIN Klinik Reichshof, Reichshof-Eckenhagen 51580, Germany*
[f] *Erwin L. Hahn Institute for Magnetic Resonance Imaging, University of Duisburg-Essen, Essen 45141, Germany*
[g] *Erasmus University College, Rotterdam 3011 HP, the Netherlands*
[h] *University Clinic and Outpatient Clinic for Radiology, Department for Radiation Medicine, University Hospital Halle (Saale), Ernst-Grube-Str. 40, Halle (Saale) 06120, Germany*
[i] *Institute of Diagnostic and Interventional Neuroradiology, Essen University Hospital, University of Duisburg-Essen, Essen 45141, Germany*
[j] *Institute of Neuroscience and Medicine (INM-1), Research Centre Juelich, Juelich 52425, Germany*
[k] *Department of Neurology, Center for Movement Disorders and Neuromodulation, Medical Faculty and University Hospital Düsseldorf, Heinrich-Heine University Düsseldorf, Düsseldorf 40225, Germany*
[l] *Institute of Clinical Neuroscience and Medical Psychology, Medical Faculty and University Hospital Düsseldorf, Heinrich-Heine University Düsseldorf, Düsseldorf 40225, Germany*
[m] *Medical Physics in Radiology, German Cancer Research Center (DKFZ), Heidelberg 69120, Germany*
[n] *Faculty of Physics and Astronomy and Faculty of Medicine, Heidelberg University, Heidelberg 69120, Germany*
[o] *Medical Physics Group, Institute of Diagnostic and Interventional Radiology, Jena University Hospital, Jena 07743, Germany*

ARTICLE INFO

Keywords:
MRI
Ataxia
Spinocerebellar ataxia type 6
Cerebellum
Quantitative susceptibility mapping
Dentate nucleus

ABSTRACT

Understanding cerebellar alterations due to healthy aging provides a reference point against which pathological findings in late-onset disease, for example spinocerebellar ataxia type 6 (SCA6), can be contrasted. In the present study, we investigated the impact of aging on the cerebellar nuclei and cerebellar cortex in 109 healthy controls (age range: 16 – 78 years) using 3 Tesla magnetic resonance imaging (MRI). Findings were compared with 25 SCA6 patients (age range: 38 – 78 years). A subset of 16 SCA6 (included: 14) patients and 50 controls (included: 45) received an additional MRI scan at 7 Tesla and were re-scanned after one year. MRI included T1-weighted, T2-weighted FLAIR, and multi-echo T2*-weighted imaging. The T2*-weighted phase images were converted to quantitative susceptibility maps (QSM). Since the cerebellar nuclei are characterized by elevated iron content

Abbreviations: BW, band width; DN_{bulk}, volume-of-interest reflecting the bulk of the iron-rich region of the dentate nucleus; DN_{sil}, volume-of-interest reflecting the silhouette of the dentate nucleus; DCN, deep cerebellar nuclei; GM, gray matter; GRE, gradient echo; FA, flip angle; FLAIR, fluid-attenuated inversion recovery; HEIDI, homogeneity-enabled incremental dipole inversion; MP-RAGE, magnetization prepared rapid gradient echo; MRI, magnetic resonance imaging; ppb, parts-per-billion; QSM, quantitative susceptibility mapping; R, parallel imaging undersampling factor; SCA6, spinocerebellar ataxia type 6; SHARP, sophisticated harmonic artifact removal for phase data; SWI, susceptibility weighted imaging; T1w, T1-weighted; TA, acquisition time; TE, echo time; TI, inversion time; TR, repetition time; VBM, voxel-based morphometry; WM, white matter.

☆ Unfortunately, the imaging data cannot be made publicly available because of privacy issues. Data derived from the images, clinical scores and demography is available from the corresponding author upon reasonable request.

* Corresponding author at: University Clinic and Outpatient Clinic for Radiology, Department for Radiation Medicine, University Hospital Halle (Saale), Ernst-Grube-Str. 40, Halle (Saale) 06120, Germany.
E-mail address: andreas.deistung@uk-halle.de (A. Deistung).

https://doi.org/10.1016/j.neuroimage.2023.119950.
Received 14 October 2022; Received in revised form 6 February 2023; Accepted 15 February 2023
Available online 22 February 2023.

with respect to their surroundings, two independent raters manually outlined them on the susceptibility maps. T1-weighted images acquired at 3T were utilized to automatically identify the cerebellar gray matter (GM) volume. Linear correlations revealed significant atrophy of the cerebellum due to tissue loss of cerebellar cortical GM in healthy controls with increasing age. Reduction of the cerebellar GM was substantially stronger in SCA6 patients. The volume of the dentate nuclei did not exhibit a significant relationship with age, at least in the age range between 18 and 78 years, whereas mean susceptibilities of the dentate nuclei increased with age. As previously shown, the dentate nuclei volumes were smaller and magnetic susceptibilities were lower in SCA6 patients compared to age- and sex-matched controls. The significant dentate volume loss in SCA6 patients could also be confirmed with 7T MRI. Linear mixed effects models and individual paired t-tests accounting for multiple comparisons revealed no statistical significant change in volume and susceptibility of the dentate nuclei after one year in neither patients nor controls. Importantly, dentate volumes were more sensitive to differentiate between SCA6 (Cohen's $d = 3.02$) and matched controls than the cerebellar cortex volume ($d = 2.04$). In addition to age-related decline of the cerebellar cortex and atrophy in SCA6 patients, age-related increase of susceptibility of the dentate nuclei was found in controls, whereas dentate volume and susceptibility was significantly decreased in SCA6 patients. Because no significant changes of any of these parameters was found at follow-up, these measures do not allow to monitor disease progression at short intervals.

1. Introduction

The aging healthy brain undergoes various structural alterations leading to impairments in executing movements and learning new movements (Seidler et al., 2010), as well as cognitive decline (Li et al., 2001; Park and Reuter-Lorenz, 2009). It is well known that the cerebellum and the cerebellar white matter (WM) tissue degenerate during aging of healthy adults (Han et al., 2020; Hoogendam et al., 2012; Koppelmans et al., 2015; Raz et al., 2001; Sullivan and Pfefferbaum, 2006). Imaging studies have also shown that volumes of cerebellar gray and white matter are reduced in elderly people (Hoogendam et al., 2012; Hulst et al., 2015; Jernigan et al., 2001). Especially, the anterior lobe of the cerebellum (lobules I–V) exhibits reduced neuronal cell count (Andersen et al., 2003) and reduced volume (Bernard and Seidler, 2013) with increasing age. The posterior lobe of the cerebellum (lobules VI–X) is also affected by aging (Dimitrova et al., 2008; Paul et al., 2009), though this relationship is not as strong as in the anterior lobe. Age-related degeneration of the cerebellum likely has an effect on behaviors associated with cerebellar function, i.e. motor behaviors (Trewartha et al., 2014) and cognitive behaviors (Bernard and Seidler, 2014; MacLullich et al., 2004).

Apart from all these studies of aging induced effects in the cerebellar cortex and white matter, little is known about the involvement of the deep cerebellar nuclei in aging. More than 60 years ago, Höpker (1951) reported volume decreases of the dentate nuclei with increasing age using histological methods in postmortem brains. He obtained volumes of the dentate nuclei ranging between 320 and 420 mm^3 for adults, whereas individuals older than 70 years exhibited volumes between 200 mm^3 and 300 mm^3, representing a decrease by approximately 30% in the elderly. Histopathological studies reported increased iron concentration in the dentate nucleus compared to the surrounding WM tissue (Benkovic and Connor, 1993; Drayer et al., 1986; Koeppen et al., 2012) as well as evaluated iron content for elderly (Hallgren and Sourander, 1958; Ramos et al., 2014). Utilizing the elevated iron levels in the dentate as a source of contrast in magnetic resonance imaging (MRI), *in vivo* studies could confirm increasing iron concentrations in the dentate nucleus over the lifespan (Aoki et al., 1989; Bilgic et al., 2012; Ghassaban et al., 2018; Li et al., 2014; Maschke et al., 2004). In addition to the dentate nuclei, elevated amounts of iron were also identified in histological stains for the globose, emboliform and fastigial nuclei relative to their surrounding tissue (Benkovic and Connor, 1993).

Understanding brain alterations due to healthy aging is of interest as it provides a reference point against which pathological findings can be contrasted. Spinocerebellar ataxias, for instance, represent a group of rare hereditary neurodegenerative disorders that go along with damages in the cerebellum and its pathways (Klockgether, 2011). Age-related alterations are of special interest in late-onset disease, such as, for example, spinocerebellar ataxia type 6 (SCA6). In contrast to many forms of hereditary ataxias, pathology in SCA6 is mostly confined to the cerebellum (Schöls et al., 2004). Clinically, SCA6 manifests commonly with a late onset around the sixth decade. Slowly progressing gait ataxia, oculomotor disorders and dysarthria are central symptoms (Schöls et al., 1998). Histological studies concerning structural alterations in SCA6 are inconsistent. While some older studies found mainly a degeneration of the cortex with little or no pathology in the deep cerebellar nuclei (DCN) (Koeppen, 2005; Sasaki et al., 1998), later observations suggested possible alterations in the DCN (Gierga et al., 2009; Wang et al., 2010).

Susceptibility weighted MR imaging (SWI) (Haacke et al., 2004; Reichenbach and Haacke, 2001) with high spatial-resolution at ultra-high magnetic fields ($B_0 \geq 7T$) offers a detailed non-invasive view of the DCN in healthy controls (Diedrichsen et al., 2011; Maderwald et al., 2012) and SCA6 patients (Stefanescu et al., 2015). Stefanescu et al. (2015) reported severe atrophy of the dentate nuclei in SCA6 patients that was even more striking than in SCA3 and Friedreich ataxia patients. With quantitative susceptibility mapping (QSM), the logical successor of SWI that directly maps the distribution of the magnetic susceptibility across the human brain, exquisite contrast and detail of the DCN has been demonstrated (Deistung et al., 2016; Li et al., 2015) at the clinically available MRI field strength of 3T. While accurate identification of iron containing structures may be impaired on SWI due to blooming and non-local phase contributions, QSM is expected to overcome those drawbacks, providing a local view of the anatomy (Deistung et al., 2013) and a more direct link to the underlying iron concentration (Hametner et al., 2018; Langkammer et al., 2012; Zheng et al., 2013).

In the present study, we investigated the influence of healthy aging on DCN and the cerebellar cortex in healthy controls based on MRI, and compared the outcome to a previously published data set in patients suffering from SCA6 (Deistung et al., 2022). A comparison of physiological alterations during the normal aging process with alterations under the influence of SCA6 as a neurodegenerative disease might help to better understand the pathophysiology of hereditary ataxias and to facilitate interpretation of MRI data in a clinical context. We assessed cross-sectional and longitudinal structural changes of the DCN and cerebellar cortex in both SCA6 and healthy subjects at magnetic field strengths of 3T and 7T.

2. Material and methods

2.1. Subjects

The study was approved by the internal Ethics Committees of the Essen University Hospital and the Jena University Hospital. Written informed consent was obtained from all participating subjects. Twenty-

Table 1
Overview of the study population. Statistics for disease duration and disease onset of the SCA6 group were only calculated for 23 and 12 patients at 3T and 7T, respectively, because one patient was not aware of the exact start of the disease and another patient did not show any symptoms at the time of data collection. For the 1 year follow-up, the latter exhibited first symptoms and was included in the statistics. One patient was excluded from the descriptive statistics of the clinical ataxia scores because of a confounding comorbidity.

	age study		group study: SCA6 vs.controls			
	baseline		baseline		follow-up	
MRI field strength	3T	7T	3T	7T	3T	7T
Control subjects						
N	109	45	25	14	17	12
age (years)	45.1 (17 – 78)	47.5 (22 – 77)	60.1 (36–78)	55.9 (36–74)	55.2 (36–74)	54.4 (36–74)
sex (m/f)	56/53	28/17	15/10	10/4	11/6	9/3
visit interval (days)					352.7 (321–384)	359.0 (321–386)
SARA (0–40)			**0.16 (0 - 1)**	**0.07 (0–1)**	**0**	**0.09 (0 - 1)**
SCAFI (z-score)			**−0.3 (−1.7 - 0.9)**	**−0.1 (−1.3 - 1.0)**	**−0.1 (−1.7 – 0.9)**	**−0.1 (−1.5 - 0.9)**
SCA6 patients						
n			25	14	17	12
age (years)			61.6 (38–79)	58.5 (39–79)	57.5 (39–76)	56.4 (39–75)
sex (m/f)			15/10	10/4	11/6	9/3
visit interval (days)					374.5 (343–504)	367.6 (357–392)
disease duration (years)			11.3 (1–25)	10.5 (3–24)	12.4 (0.3–26)	10.9 (0.3–25)
SARA (0–40)			**13.3 (0.5–26)**	**12.8 (0.5–24)**	**13.0 (0.5–26)**	**13.8 (0.5–26)**
SCAFI (z-score)			**−2.7 (− 5.3- − 0.4)**	**−2.4 (− 4.4- − 0.4)**	**−2.5 (− 4.2–0.09)**	**−2.4 (− 4–0.1)**
CAG repeats (short)			12.4 (10–13)	12.1 (10–13)	12.2 (10–13)	12.2 (10–13)
CAG repeats (long)			22.4 (21–27)	22.4 (21–27)	22.5 (21–27)	22.4 (21–27)

The cell entries with brackets are mean (minimum - maximum) across the cohort. SARA – Scale for the Assessment and Rating of Ataxia. SCAFI – SpinoCerebellar Ataxia Functional Index. Statistical significance ($p < 0.001$) between SCA6 and the matched controls assessed using two-sampled *t*-test is indicated by bold font. There were no statistical significances of age between the patient and control groups.

five SCA6 patients as well as 126 healthy controls underwent 3T-MRI and clinical assessments at least once. Among the participants included, 16 SCA6 patients and 50 controls additionally received a 7T-MRI scan. Nineteen SCA6 patients (3T: 19, 3T and 7T: 14) and 33 controls (3T: 33, 3T and 7T: 22) received a one-year follow-up examination. The healthy controls served to study age-related alterations of the cerebellum. In addition, a subset was selected that was age- and sex-matched to the SCA6 group. The demographic and clinical details of all included participants are summarized in Table 1 (see Supplementary Section S1 for details on exclusion of participants). Data (cerebellar volume as well as volume, susceptibility and susceptibility mass of dentate nuclei, SARA) of the subgroup of SCA6 patients and the corresponding controls acquired during the first 3T examination, has been presented partly in Deistung et al., 2022. Employed statistical analysis methods, however, were different in the present work.

All patients had genetically proven disease. The CAG repeat length and disease duration were recorded. Clinical ataxia scores were assessed based on the Scale for the Assessment and Rating of Ataxia (SARA) (Schmitz-Hubsch et al., 2006), and the SpinoCerebellar Ataxia Functional Index (SCAFI) (Schmitz-Hubsch et al., 2008b). SARA (range: 0–40) is a sum score and increases the more severe the degree of ataxia. The SCAFI represents the sum of the z-scores of an 8 m walk test, a 9-hole peg-test, and a speech test, where the individual z-scores were calculated with respect to the corresponding mean values of our healthy control group (n = 109). Consequently, the SCAFI deviates from zero the more the subject's values deviate from the average of the healthy control population. A negative SCAFI indicates a decreased performance of the tasks in relation to the healthy control group. The lower the SCAFI, the worse the performance.

2.2. MRI data acquisition

MRI data of all patients and the majority of controls (n = 106) were collected with a human whole-body combined MRI-PET system (Siemens Healthineers, Erlangen, Germany), operating at a magnetic field strength of 3T, by using a 16-channel head array coil (Siemens Healthineers). Further, 20 controls (all of them were included in the analysis of age-related effects) underwent 3T-MRI on a PRISMA Fit (Siemens Healthineers) equipped with a 64-channel head array coil (Siemens Healthineers). The same acquisition protocols were used for the two 3T-MRI systems. Multi-echo, three-dimensional (3D) gradient-echo (GRE) imaging was carried out in transverse-to-coronal orientation for subsequent quantitative susceptibility mapping. To this end, four echoes with monopolar read-out were recorded (TE_{1-4} = 6.47 ms/17.23 ms/27.99 ms/38.75 ms, TR=62 ms, flip angle (FA)=17°, BW_{1-4} = 120 Hz/px, phase encoding direction: right/left, acquisition matrix = 384 × 324 × 160) with an interpolated voxel size of 0.5 mm × 0.5 mm × 0.5 mm in an acquisition time (TA) of 13:09 min:sec. Data were collected with partial parallel undersampling (GRAPPA) with an undersampling factor (R) of 2 and 48 reference lines along the phase encoding direction and 75% partial Fourier along the slice encoding direction. Both phase resolution and slice resolution were adjusted to 74% to further reduce acquisition time, resulting in an acquired voxel size of 0.5 mm × 0.67 mm × 0.67 mm. Saturation pulses were positioned inferior and superior to the field-of-view (FoV) to avoid non-local artifacts due to pulsatile blood flow in vessels close to the cerebellum. In addition, whole-head T1-weighted (T1w) MRI data sets were collected with a magnetization prepared rapid gradient echo (MP-RAGE) sequence for determining the total intracranial volume (TIV) and automatically identifying the cerebellar lobules. The T1w data were acquired in sagittal orientation with an isotropic voxel size of 1 mm, TE=3.26 ms, TR=2530 ms, inversion time (TI)=1100 ms, FA=7°, acquisition matrix = 256 × 256 × 176, BW = 200 Hz/Px, GRAPPA with R = 2 and 48 reference lines, resulting in an acquisition time of 6:24 min:sec. Finally, fluid-attenuated inversion recovery (FLAIR) images covering the whole brain were acquired using a 2D sequence with TI = 2500 ms, TE = 94 ms, TR = 9000 ms, FA = 150°, acquisition matrix = 256 × 208, 55 contiguous slices and an acquired voxel size of 0.9 mm × 0.9 mm × 3 mm that was interpolated to 0.45 mm × 0.45 mm × 3 mm. MPRAGE and FLAIR images were inspected by a neuroradiologist (SLG). Controls were excluded from the study in case cerebral abnormalities were identified.

To validate the features and appearances detected on 3T-MR images, we carried out additional MRI exams of 16 patients and 50 controls on a 7T whole-body MRI system (Siemens Magnetom 7T, Siemens

Healthineers) using a 32-channel head array coil (NOVA Medical Inc., Wilmington, MA, USA). The lower coil was covered with two dielectric pads (dimensions: 170 mm × 110 mm × 10 mm, provided by the Leiden Medical Center [Leiden, The Netherlands]) made of calcium titanate ($CaTiO_3$, permittivity: 110, loss tangent: 0.05) to increase both field strength and homogeneity of the transmit radiofrequency field, B_1^+, in the area of the cerebellum. Gradient-echo images for QSM were acquired with 4 echoes (TE_{1-4} = 4.49 ms/11.23 ms/17.97 ms/24.71 ms, BW_{1-4} = 280 Hz/px, monopolar echo readout, TR = 30 ms, FA = 10°) and an isotropic voxel size of 0.38 mm (matrix: 552 × 552 × 192, GRAPPA with R = 3 and 48 reference lines in phase encoding direction, 75% partial Fourier in slice encoding direction, phase-encoding direction = anterior/posterior) within an acquisition time of 16:32 min:sec. To enable retrospective correction of slight head movements, the sequence was equipped with 3D fat navigators (voxel size = 4 mm × 4 mm × 4 mmm, GRAPPA [R = 4 × 4]) (Gallichan et al., 2016). The fat navigators (n = 215) were measured after the 4th gradient-echo for each phase encoding step (phase encoding loop outside the slice encoding loop). The gradient-echo k-space data were reconstructed offline by adjusting the Matlab scripts of the retroMoCoBox (https://github.com/dgallichan/retroMoCoBox) to mitigate motion related artifacts.

2.3. MRI data processing

2.3.1. QSM

Single-channel GRE magnitude and phase images were combined using the sum-of-squares method (Roemer et al., 1990) and the MCPC-3D-S approach (Eckstein et al., 2018), respectively. A spatially adaptive non-local means denoising algorithm (Manjon et al., 2010) was applied to the real and imaginary parts of the combined complex-valued images to mitigate noise. The denoising strength (υ) was constant across the echoes of the 3T data (υ_{1-4} = 100%), but was increased with longer echo times at 7T (υ_{1-4} = 25%/50%/75%/85%). Quantitative susceptibility maps were computed based on these denoised phase images (at 3T: all echoes were considered, at 7T: only echoes 1 to 3 were considered) as described in Deistung et al., 2022. We referenced all susceptibility maps to the average susceptibility of the brain tissue within the field of view and stated susceptibility values in parts-per-billion (ppb).

Magnetic susceptibility in the DCN serves as proxy for iron concentration. Because iron concentration and thus susceptibility could be affected by atrophy, we also examined the susceptibility mass of the dentate nucleus as a measure of total tissue iron content (Hernandez-Torres et al., 2018; Schweser et al., 2021). Susceptibility mass was calculated by multiplying the non-normalized dentate nucleus volume (DN_{sil} or DN_{bulk}, definition see next subsection) by the mean susceptibility.

2.3.2. Segmentation and volume estimation

Susceptibility maps were used to demarcate the cerebellar nuclei. The cerebellar nuclei were manually traced by two independent raters, who were blinded to the diagnosis and age, following the same delineation strategy. Data obtained from the SCA6 patients and matched controls were demarcated two times by the raters. If clearly discernible, the DCN were manually traced in both hemispheres on the axial, sagittal and coronal susceptibility maps using MRICroN (http://people.cas.sc.edu/rorden/mricron/). Drawings were done directly on the susceptibility maps taking into account information of gradient-echo magnitude images and processed phase images (corrected for contributions originating from sources outside the brain) as well. In line with Deistung et al., 2022, two different volumes of interest (VOIs) were created for the dentate nucleus. The first VOI was manually traced and followed the silhouette that is the corrugated wall of the dentate nucleus (silhouette, DN_{sil}) as well as possible and is motivated by the anatomical structure of the dentate nucleus. The second dentate VOI (DN_{bulk}) represents the convex hull obtained from the first manually traced VOI and, thus additionally included the white matter surrounded by the corrugated wall of the dentate nucleus. Hence, DN_{bulk} more closely reflects the visual appearance of the dentate area on susceptibility maps including the high susceptibilities within the cortical ribbon. More details on the definition of DN_{sil} and DN_{bulk} are available in Deistung et al., 2022. The absolute volumes were determined for each cerebellar nucleus. Dentate VOIs specified by the first demarcation of rater 1 were used to study age-related effects and to investigate changes between SCA6 and controls. In the case of multiple examinations of a person (baseline vs. follow-up or 3T vs. 7T), the cerebellar nuclei segmentations were carried out by treating each data set as independent measurement. The surface area of the dentate was computed based on the binary representation of DN_{sil} using the MatImage library (http://github.com/mattools/matImage) (Legland et al., 2007).

Subject-specific segmentations of cerebral and cerebellar structures were generated by Freesurfer's (https://surfer.nmr.mgh.harvard.edu/, version 6.0) automatic processing pipeline for T1w data (Destrieux et al., 2010; Fischl et al., 2002). If the study participants were measured at baseline and 1 year follow-up, the corresponding T1w data were processed using Freesurfer's longitudinal stream (Reuter et al., 2012). The resulting segmentation of the cerebellum was further refined using an automated cerebellar lobule segmentation method that relies on the incorporation of multi-atlas labeling and tissue classification outcomes in a graph cut framework (Yang et al., 2016). The absolute volumes of the individual cerebellar lobules and cerebellar white matter were calculated. The cerebellum volume was determined as the sum of all segmented cerebellar lobules, vermis, and the cerebellar white matter segment. We also computed volumes for the cerebellar GM and cerebellar cortical GM. The former was defined as the sum of the volumes of all lobules, vermis and cerebellar nuclei, whereas the latter represents only the sum of all lobules.

Three-dimensional gradient unwarping (https://github.com/Washington-University/gradunwarp) utilizing the gradient coefficient file of the corresponding MRI system has been applied to QSM and MP-RAGE data. The corresponding nonlinear deformation field has been applied to all segmentations (DN_{sil}, DN_{bulk}, cerebellar lobules) to correct for geometric distortions due to MR gradient nonlinearity.

To account for different head sizes, the absolute volumes were further processed considering the total intracranial volume (TIV) (details see below). The TIV was estimated based on the unwarped T1w images acquired at 3T using the standard pre-processing pipeline of the Computational Anatomy Toolbox 12 (CAT12, http://www.neuro.uni-jena.de/cat/).

2.4. Statistical analysis

Because of the lack of reliability observed for the emboliform, globose, and fastigial nuclei, we decided to exclude them from further analysis (see Supplementary Section S2).

To account for different head sizes, absolute volumes were corrected with respect to TIV using residualization (Sanfilipo et al., 2004; Voevodskaya et al., 2014). We selected residualization because the volumes of the dentate nuclei are very small and residualization is less affected by systematic and random errors in TIV and the individual volume that needs to be normalized. To this end, linear regressions between the absolute volumes (DN_{sil}, DN_{bulk}, cerebellar lobes, cerebellar GM and WM, cerebellum) and the TIVs calculated based on the T1-weighted data of the first 3T MRI examination of the healthy controls yielded the linear functional relationship (v(TIV)). The residuals of the individual volumes were calculated with respect to their prediction v(TIV) and standardized according to the ones of the whole sample. The prediction v(TIV) was always computed with respect to the TIV obtained from the first 3T MRI measurement to exclude influences introduced by slight variations in TIVs calculated based on the 1-year follow-up and 7T MRI data. By using the linear relationship between the VOI and TIV of the control group for the correction, it was assumed that this linear function represents the "normal" relationship between the VOI and TIV, but that this relationship is not necessarily sustained in the case of pathology.

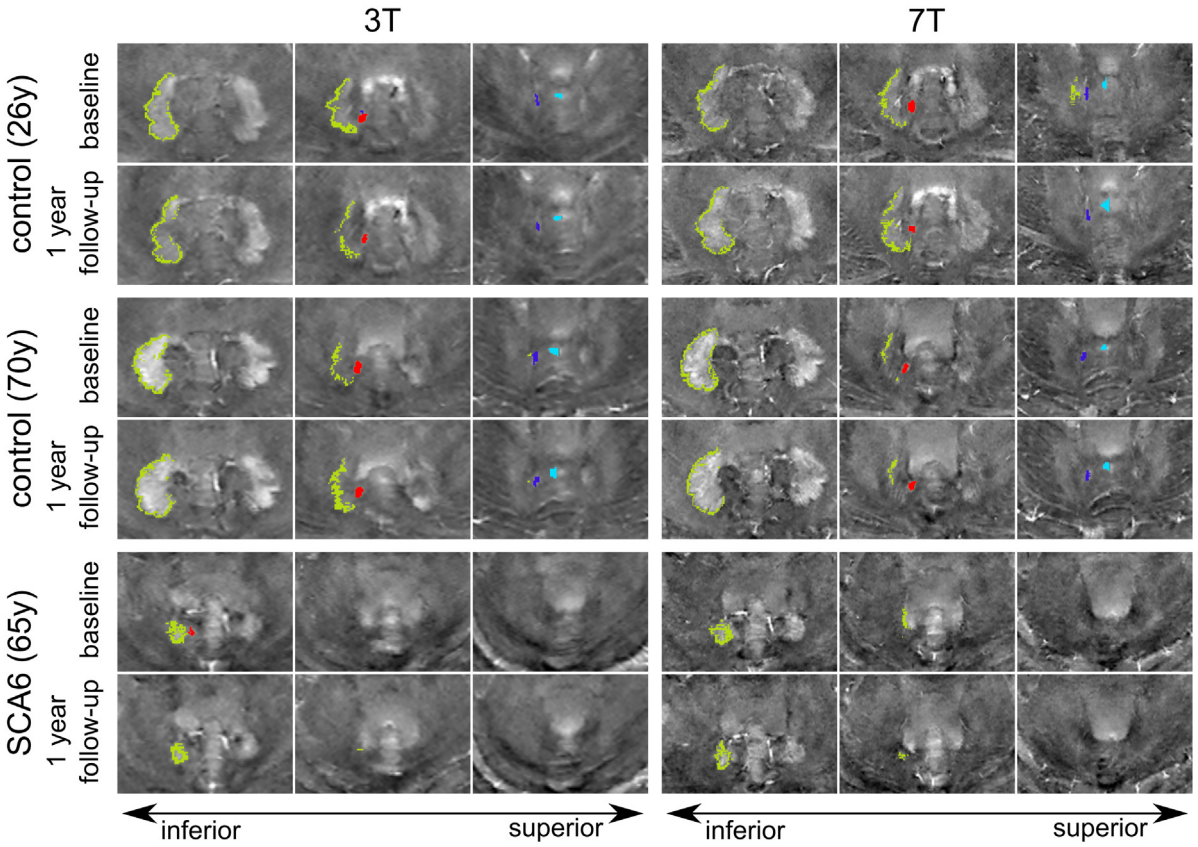

Fig. 1. Axial sections of quantitative susceptibility maps of the cerebellum of a young healthy control (male, 26y, TIV = 1685 cm^3), an elderly control (male, 70y, TIV = 1752 cm^3), and an SCA6 patient (male, 65y, TIV = 1742 cm^3) are presented from the top to the bottom row, respectively. The cerebellar nuclei of the left hemisphere are clearly seen on the maps. The manual delineations of the cerebellar nuclei are depicted for the right hemisphere (light green: dentate nucleus, red: globose nucleus, blue: emboliform nucleus, cyan: fastigial nucleus). The dentate nuclei of the SCA6 patient are substantially smaller compared to the ones of the age matched control. The emboliform, globose, and fastigial nuclei were not discernible on the maps of the SCA6 patient. As intra- and interrater comparisons yielded low reliability in the identification of the emboliform, globose, and fastigial nuclei, we decided to exclude these smaller nuclei from further analysis. An in-depth investigation of the reliability of the manually delineated cerebellar nuclei VOIs, their volumes and the average susceptibilities is given in the Supplementary Section S2.

We investigated the linear association of the (standardized) volumes of the cerebellum, cerebellar lobules, white matter and dentate nuclei, as well as surface area, magnetic susceptibility and susceptibility mass of the dentate nuclei with respect to age using linear regression models. For each metric (Y) and each specific region we set up a linear regression model with age and group (0 – controls, 1 – SCA6) as predictors taking also their interaction into account (Y ~ 1 + age + group + age * group) resulting in 24 independent comparisons. This model also enabled studying varying associations between the specific metric and age for controls and SCA6 patients. The presence of linear correlations has also been investigated independently on group, metric and region using Pearson correlations. In a further attempt, multivariate linear regressions were carried out independently for each the control group and the SCA6 patient group. Here, standardized volumes (Y) across regions were studied with a linear model of age, region and the interaction of age and region to assess whether volume associations with age are different from the one of the whole cerebellum (Y ~ 1 + age + region + age * region). Similarly, different associations with age were also studied for DN_{sil} and DN_{bulk} for each susceptibility and susceptibility mass.

For each measure (not normalized volume, susceptibility, susceptibility mass, surface area) differences between SCA6 and controls were probed using individual ANCOVAs between the group (3T vs. 7T or SCA6 vs. controls) and age as covariate. For a more detailed investigation, group comparisons based on 3T data were also conducted by fitting linear mixed effects models and calculating the estimated marginal means. Afterwards, post-hoc tests were carried out to statistically investigate the presence of group differences between SCA6 and controls and the presence of changes in measures obtained at baseline and 1-year follow up. Independent linear mixed models were set up for the volumes (obtained from nineteen regions, standardized residuals of TIV-corrected volume), the susceptibility (obtained from two regions), the susceptibility mass (obtained from two regions), and the surface area (obtained from one region) as response variable (Y). Each model included intercept, region (e.g. DN_{sil}, DN_{bulk}), group (HC and SCA6), time (baseline and follow-up) and age as fixed effects. The interactions between region and group, between region and time, between group and time, and between region, group and time were also considered as fixed effects. Region, group and time were modeled as categorical variables. The subject identifier was modeled as random effect by accounting for random intercepts with a fixed slope. Partial eta squared, η_p^2, and Cohens' d were calculated to quantify effect sizes. As the configured linear mixed models compare differences between baseline and 1 year follow-up on the group level, paired t-tests between baseline and follow-up have been applied separately for each measure.

Correlations between MRI measures, disease onset and genetics (repeat length) were calculated using Spearman correlation. Potential associations between MRI measures and SCAFI (Y) were investigated using linear regression models for each MRI measure separately. These linear models were set up to investigate differences in the slopes between controls and patients (similar to the age analysis; Y ~ 1 + age + group + age * group).

All statistical analyzes were performed with SPSS (version 28; IBM, Armonk, NY, United States), Matlab (Mathworks Inc., Natick, MA,

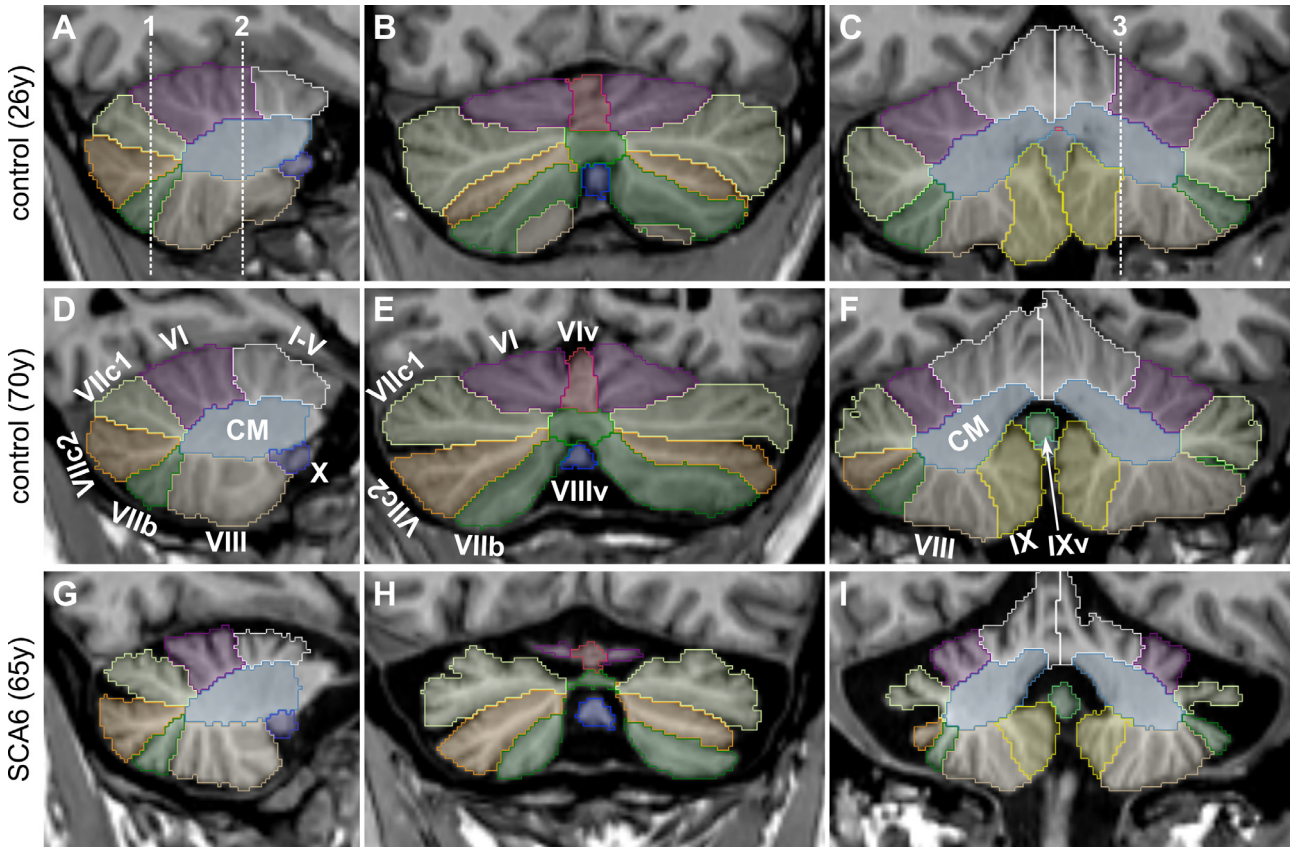

Fig. 2. T1-weighted images of the cerebellum with superimpositions of the cerebellar lobules in a young healthy control (male, 26y, TIV = 1685 cm^3), an elderly control (male, 70y, TIV = 1752 cm^3) and an SCA6 patient (male, 65y, TIV = 1742 cm^3) are presented from top to bottom row, respectively, indicating accurate segmentation across age. The left column shows the sagittal view of the cutting plane indicated by dashed line 3 in (C). The middle and right columns display coronal slices at the locations indicated by dashed line 1 and 2 in (A), respectively. The cerebellum of the SCA6 patient (G-I) exhibits considerable atrophy compared to the elderly control (D-F). The color scheme of the cerebellar segmentation is indicated in the middle row: I-V – lobules I to V, VI – lobule VI, VIv – vermis lobule VI, VIIc1 – Crus I, VIIc2 – Crus II, VIIb – lobule VIIb, VIII – lobule VIII, VIIIv – vermis lobule VIII, IX – lobule IX, IXv – vermis lobule IX, X – lobule X and CM – corpus medullare.

United States) and R (https://www.r-project.org/). Type 1 error correction for multiple comparisons was conducted using the Bonferroni-Holm approach (Holm, 1979), where appropriate. Corrected *p*-values smaller than 0.05 were considered statistically significant, while uncorrected p-values of less than 0.05 were considered a trend.

2.5. Data availability

Unfortunately, the imaging data cannot be made publicly available because of privacy issues. Data derived from the images, clinical scores and demography is available from the corresponding author upon reasonable request.

3. Results

3.1. Age dependency

Characteristic susceptibility maps and results of the automatic segmentation for the cerebellar lobules of a young control, an elderly control and an SCA6 patient are presented in Figs. 1 and 2.

Results of linear multivariate regression analyzes (r^2, coefficient estimates and standard errors) of cerebellar gray and white matter tissues, lobules and dentate nuclei volumes with respect to age are summarized in Table 2 for healthy controls and SCA6 patients. The overall quality measures (F-test, *p*-value) of the different models and the resulting regression equations are presented in Supplementary Table 4. The F-tests always revealed p-values less than 0.05 except for the volumes of the vermis of lobule IX and X. Linear correlations show a significant decline of the cerebellum due to significant tissue loss of the cerebellar GM in healthy controls with increasing age (see also Fig. 3). The volume loss of the cerebellar GM in healthy controls is mainly driven by significant tissue declines in Crus I, lobule VIIb and vermal lobule VII and to a lesser extent by tissue decline in lobules I-V, lobule VI and VIII (Table 2). In SCA6 patients, we observed cerebellar cortical GM decline with increasing age at a raw p-value of 0.052 (Supplementary Table 4) and appeared to be more pronounced than for controls (p-value of slope difference: 0.038). In patients, cerebellar GM decline is mostly driven by tissue loss in Crus I and lobule VIII as indicated by statistically significant correlations when only accounting for the SCA6 patients (Supplementary Table 4).

The volumes of DN_{sil} (Fig. 3D) and DN_{bulk} as well as the surface area of DN_{sil} did not exhibit a significant relationship with age neither in healthy controls nor in patients (Supplementary Table 4).

Magnetic susceptibility and susceptibility mass of DN_{bulk} are presented as functions of age in Fig. 3E and F. In healthy controls, mean susceptibilities and susceptibility mass of the dentate nuclei significantly increased with age. While the multivariate linear model suggested a different slope for SCA6 patients compared to controls (Table 2), no significant correlation was observed when inspecting SCA6 patients with increasing age in a univariate analysis (Supplementary Table 4). The same holds true for the volume and surface area of the dentate.

Analyzing the multivariate linear models incorporating different regions of the volumes suggested a statistically significant different slope in comparison to the one of the whole cerebellum ($-7.2e^{-3}$) for the ver-

mis of lobule X (p-corrected = 0.0002, slope: 0.013) as well as a trend for the vermal lobule IX (raw p-value: 0.021, slope: 0.0033), lobule X (raw p-value: 0.004, slope: 0. 006) and DN_{bulk} (raw p-value: 0.029, slope: 0.0028) in healthy controls. In the SCA6 group, a trend for a varying slope of the vermis of lobule X (raw p-value: 0.025, slope: 0.022) with respect to the one of the whole cerebellar volume (-0.023) was found, whereas the slopes of the other 17 cerebellar structures did not show a statistically significant deviation from the cerebellar volume slope. In healthy controls, slopes of susceptibility and susceptibility mass were higher for DN_{bulk} (susceptibility: $p = 0.0015$, slope: 0.72; susceptibility mass: $p < 0.001$, slope: 1.33) than for DN_{sil} (susceptibility: slope: 0.22, susceptibility mass: slope: 0.16).

3.2. Group comparisons

3.2.1. Baseline measurements

Note that selected 3T baseline measures (cerebellum volume as well as volumes, susceptibility, and susceptibility mass for the two dentate definitions) for SCA6 patients and matched controls have already been published without gradient nonlinearity correction in (Deistung et al., 2022). In brief, volumes of the cerebellar nuclei are summarized for both controls and SCA6 patients in Table 3 and Fig. 4**.** The whole cerebellum, the cerebellar GM, the cerebellar cortex and the cerebellar WM exhibited significantly reduced volumes in SCA6 patients compared to age- and sex-matched healthy controls. A closer look into the substructure of the cerebellar cortex revealed a significant volume loss of all individual cerebellar and vermal lobules in SCA6 patients, with the exception of the vermal lobule X (Fig. 5). Volumes of DN_{sil} and DN_{bulk} were significantly smaller in SCA6 patients with effect sizes (Cohen's d) above 3. The effect is even more pronounced when inspecting the surface area of DN_{sil} ($d = 12.9$) (Fig. 4B).

Magnetic susceptibilities and susceptibility masses of the dentate are presented for controls and SCA6 patients in Fig. 4C and D. DN_{sil} exhibited significantly lower values of the magnetic susceptibility ($d = 1.54$) and susceptibility mass ($d = 0.87$) in SCA6 patients. The effect size was substantially higher when comparing the difference of susceptibility mass of DN_{bulk} between SCA6 and controls ($d = 3.55$) and slightly lower for the susceptibility of DN_{bulk} ($d = 1.31$). The differences between controls and SCA6 patients revealed by the susceptibility, susceptibility mass and surface area of the dentate nuclei observed at 3T are supported by the measurements at 7T (Table 3). A more detailed comparison between 3T and 7T measures is provided in Supplementary Section 4.

3.2.2. Longitudinal changes

The SARA score increased by 1.06 (standard error [SE] = 0.88) in the group of SCA6 patients (n = 17) who were tested for follow-up at 3T and by 0.73 (SE = 0.61) in the subgroup with follow-up at 7T ($n = 12$)].

TIV-corrected volumes of cerebellar regions, as well as surface area, susceptibility and susceptibility mass are presented for baseline and 1-year follow up in Figs. 4 and 5. The linear mixed model for the TIV-corrected volumes (19 regions: $DN_{sil,}$ DN_{bulk}, whole cerebellum, cerebellar GM and WM, lobules, vermis) did not show a significant main effect of time between baseline and 1 year follow up for both SCA6 (uncorrected $p = 0.47$) and matched controls (uncorrected $p = 0.75$). Likewise, paired t-tests applied for each region separately in either SCA6 patients or controls and considering multiple hypothesis testing using the Bonferroni-Holm approach did not indicate significant volume changes after 1 year follow-up (corrected $p > 0.05$, Supplementary Tables 5, Fig. 4). As comparison, volumes and surface areas represented as absolute values are summarized in Supplementary Fig. 2 and Supplementary Table 6. The statistical analysis based on the absolute volumes supports the outcome obtained with the TIV-corrected values.

The fitted linear mixed effects models for susceptibility, susceptibility mass and surface area did not exhibit a significant change between baseline and 1-year follow-up for both SCA6 and controls (all p values > 0.05). Contrary, paired t-tests indicated lower values after 1 year follow-up for the susceptibility mass and surface area in SCA6 patients as well as susceptibility mass of DN_{sil} in the controls (Supplementary Tables 5 and 6, Fig. 4). The uncorrected p-values of the susceptibility mass were in a range of 0.01 and 0.025.

For the patients, the intraclass correlation coefficient (ICC) computed for the various metrics between baseline and follow-up always exceeded 0.87 (lowest ICC of 0.873 was observed for the volume of lobule X). The intraclass correlation coefficients of the control group were slightly lower than for the SCA6 group (Supplementary Tables 5 and 6).

3.3. Correlation with clinical scores

Within the group of healthy controls ($n = 109$), SCAFI correlated with volumes of the whole cerebellum and cerebellar GM but not with the one of DN_{sil} (Fig. 6). Linear regression modeling revealed statistically significant varying slopes between SCAFI and cerebellar volume (incorporating age: $d = 2.2$, $p < 0.001$, neglecting age: $d = 1.58$, $p < 0.001$) as well as SCAFI and cerebellar cortical GM for healthy controls and SCA6 patients (incorporating age: $d = 2.1$, $p < 0.001$, neglecting age: $d = 1.45$, $p < 0.001$). An in-depth linear mixed effects model analysis of volume measures and surface area of the SCA6 patients with respect to either SCAFI or SARA considering age as covariate can be found in Supplementary Section S6.

No significant linear relationships between the volumes of the whole cerebellum and selected cerebellar structures (lobules, nuclei, GM, WM) as well as susceptibility of the dentate were observed with respect to the CAG repeat length or the disease duration. The lack of correlation with CAG repeat length is not surprising due to its small variation in SCA6 patients. The CAG repeat length in the pathological allele correlated significantly with the age of the initial clinical disease manifestation (Spearman $r = 0.546$, $p = 0.006$), indicating that a higher number of CAG repeats in the elongated (i.e. disease determining) allele leads to an earlier onset. No correlation was found for the number of repeats in the non-affected allele.

4. Discussion

We investigated the cerebellum and its substructures non-invasively in healthy aging controls and in SCA6 patients. While the volume of the dentate nuclei did not significantly vary with age, the magnetic susceptibility and therefore iron concentration of the dentate nuclei significantly increase during the lifespan. The decrease in volume of the entire cerebellum and selected cerebellar lobules with increasing age was confirmed. As shown previously, the volumes of the dentate nuclei were smaller in SCA6 patients compared to age- and sex-matched controls. In addition, lower magnetic susceptibilities and susceptibility masses were found in the dentate nuclei in the group of all SCA6 patients. After one year, neither patients nor controls showed significant changes of the volume and susceptibility. Cerebellar GM and dentate volumes significantly correlated with clinical ataxia scores.

4.1. Age dependency

We verified a loss of cerebellar volume with increasing age in healthy subjects, which was mainly due to a decline of cortical gray matter (Bernard and Seidler, 2013). The volume reduction with increasing age was mostly driven by the decline of cortical GM in Crus I (as part of lobule VIIa), lobule VIIb and vermal lobule VII as well as to a lesser extent in lobules I-V, VI and VIII. This finding is in agreement with Bernard and Seidler (2013), who observed gray matter volume loss mainly in the anterior lobe and Crus I when comparing young (age: 22.04 ± 3.47 years) with elderly subjects (age: 65.03 ± 6.42 years) using the SUIT-approach (Diedrichsen, 2006; Diedrichsen et al., 2009). By analyzing T1w images from the OASIS database, which contained 313 subjects ranging from 18 to 97 years, with voxel-based morphometry

Table 2
Results of the linear models with volume, surface, susceptibility or susceptibility mass as response variable and age and group as main effects and the interaction between both. Further quality metrics (F and p-value) of the respective linear model as well as the resulting slopes for the individual groups are specified in Supplementary Table 4. The F-tests between the individual specific model and a degenerated model consisting only a constant term always revealed *p*-values less than 0.05 except for the volumes of the vermis of lobule IX and X (Supplementary Table 4).

		intercept (control group)			Age (control group)			difference to intercept of controls (patient group)			difference to age slope of controls (patient group)		
	r^2	*β*	SE	p	*β*	SE	p	*β*	SE	p	*β*	SE	p
volume													
cerebellum	0.648	**0.325**	**0.100**	**1.5e^{-3}**	**−7.2e^{-3}**	**2.1e^{-3}**	**7.0e^{-4}**	−0.129	0.453	0.77	**−0.016**	**7.3e^{-3}**	**0.031**
cerebellar WM	0.213	−0.045	0.090	0.621	1.0e^{-3}	1.9e^{-3}	0.596	0.219	0.409	0.593	−0.011	6.7e^{-3}	0.105
cerebellar GM[1]	0.650	**0.365**	**0.105**	**7.1e^{-4}**	**−8.1e^{-3}**	**2.1e^{-3}**	**2.9e^{-4}**	−0.174	0.474	0.715	**−0.015**	**7.7e^{-3}**	**0.039**
cerebellar cortical GM[2]	0.637	**0.382**	**0.107**	**5.2e^{-4}**	**−8.4e^{-3}**	**2.2e^{-3}**	**2.0e^{-4}**	−0.118	0.485	0.808	**−0.017**	**7.8e^{-3}**	**0.038**
lobule I-V	0.455	**0.272**	**0.120**	**0.026**	**−6.0e^{-3}**	**2.5e^{-3}**	**0.017**	−0.545	0.544	0.318	−0.013	8.8e^{-3}	0.147
lobule VI vermis	0.294	0.176	0.179	0.326	−3.9e^{-3}	3.7e^{-3}	0.293	−0.953	0.808	0.240	−1.1e^{-3}	0.013	0.931
lobule VI	0.506	**0.311**	**0.139**	**0.027**	**−6.8e^{-3}**	**2.9e^{-3}**	**0.018**	−0.706	0.631	0.265	−7.9e^{-3}	0.010	0.443
lobule VII vermis	0.350	**0.427**	**0.172**	**0.015**	**−9.5e^{-3}**	**3.6e^{-3}**	**9.0e^{-3}**	−0.841	0.780	0.283	−2.3e^{-3}	0.013	0.856
Crus I	0.410	**0.567**	**0.154**	**3.6e^{-4}**	**−0.013**	**3.2e^{-3}**	**1.3e^{-4}**	0.443	0.699	0.527	−0.021	0.011	0.069
Crus II	0.184	0.139	0.191	0.470	−3.1e^{-3}	4.0e^{-3}	0.439	−0.116	0.867	0.893	−0.011	0.014	0.437
lobule VIIb	0.382	**0.426**	**0.160**	**8.7e^{-3}**	**−9.4e^{-3}**	**3.3e^{-3}**	**5.5e^{-3}**	−0.558	0.722	0.441	−6.6e^{-3}	0.012	0.574
lobule VIII vermis	0.409	0.175	0.144	0.230	−3.9e^{-3}	3.0e^{-3}	0.198	**−1.568**	**0.650**	**0.017**	8.0e^{-3}	0.011	0.450
lobule VIII	0.510	**0.288**	**0.129**	**2.8e^{-2}**	**−6.3e^{-3}**	**2.7e^{-3}**	**1.9e^{-2}**	0.349	0.584	0.552	**−0.023**	**9.5e^{-3}**	**0.016**
lobule IX vermis	0.031	−0.151	0.230	0.513	3.4e^{-3}	4.8e^{-3}	0.483	2.5e^{-3}	1.040	0.998	−6.9e^{-3}	0.017	0.684
lobule IX	0.118	0.239	0.203	0.240	−5.3e^{-3}	4.2e^{-3}	0.208	0.375	0.916	0.683	−0.015	0.015	0.319
lobule X vermis	0.056	**−0.583**	**0.254**	**0.024**	**0.013**	**5.3e^{-3}**	**0.015**	−0.709	1.148	0.538	9.1e^{-3}	0.019	0.625
lobule X	0.116	−0.270	0.248	0.278	6.0e^{-3}	5.1e^{-3}	0.244	−1.04	1.18	0.355	2.0e^{-3}	0.018	0.912
DN_{sil}	0.639	−0.038	0.127	0.768	8.3e^{-4}	2.6e^{-3}	0.751	−0.161	0.571	0.778	**−0.023**	**9.3e^{-3}**	**0.014**
DN_{bulk}	0.595	−0.125	0.143	0.383	2.8e^{-3}	3.0e^{-3}	0.350	−0.025	0.645	0.970	**−0.027**	**0.010**	**0.012**
surface area													
DN_{sil}	0.662	−0.039	0.133	0.771	8.5e^{-4}	2.7e^{-3}	0.755	−0.144	0.599	0.742	**−0.026**	**9.7e^{-3}**	**0.008**
susceptibility													
DN_{sil}	0.150	**45.90**	**4.297**	**1.6e^{-19}**	**0.217**	**0.089**	**0.016**	16.91	19.39	0.385	−0.563	0.315	0.076
DN_{bulk}	0.176	**51.51**	**6.841**	**7.5e^{-12}**	**0.716**	**0.141**	**1.3e^{-6}**	**68.58**	**30.90**	**0.029**	**−1.358**	**0.502**	**7.7e^{-3}**
susceptibility mass													
DN_{sil}	0.351	**30.19**	**3.456**	**1.0e^{-14}**	**0.159**	**0.071**	**0.027**	6.694	15.60	0.668	**−0.524**	**0.253**	**0.041**
DN_{bulk}	0.359	**73.38**	**14.25**	**9.5e^{-7}**	**1.325**	**0.295**	**1.5e^{-5}**	89.43	64.33	0.167	**−3.165**	**1.045**	**3.0e^{-3}**

r^2 – coefficient of determination. *β* - fixed effect coefficients. SE - standard error. p - raw p value (without any correction for multiple comparisons). Effects with a raw p-value < 0.05 are printed bold. [1] – volume of the whole GM including vermis and cerebellar nuclei. [2] – volume of the cerebellar cortical GM excluding the vermis. DN_{sil} – silhouette of dentate nuclei. DN_{bulk} – bulk of the dentate nuclei.

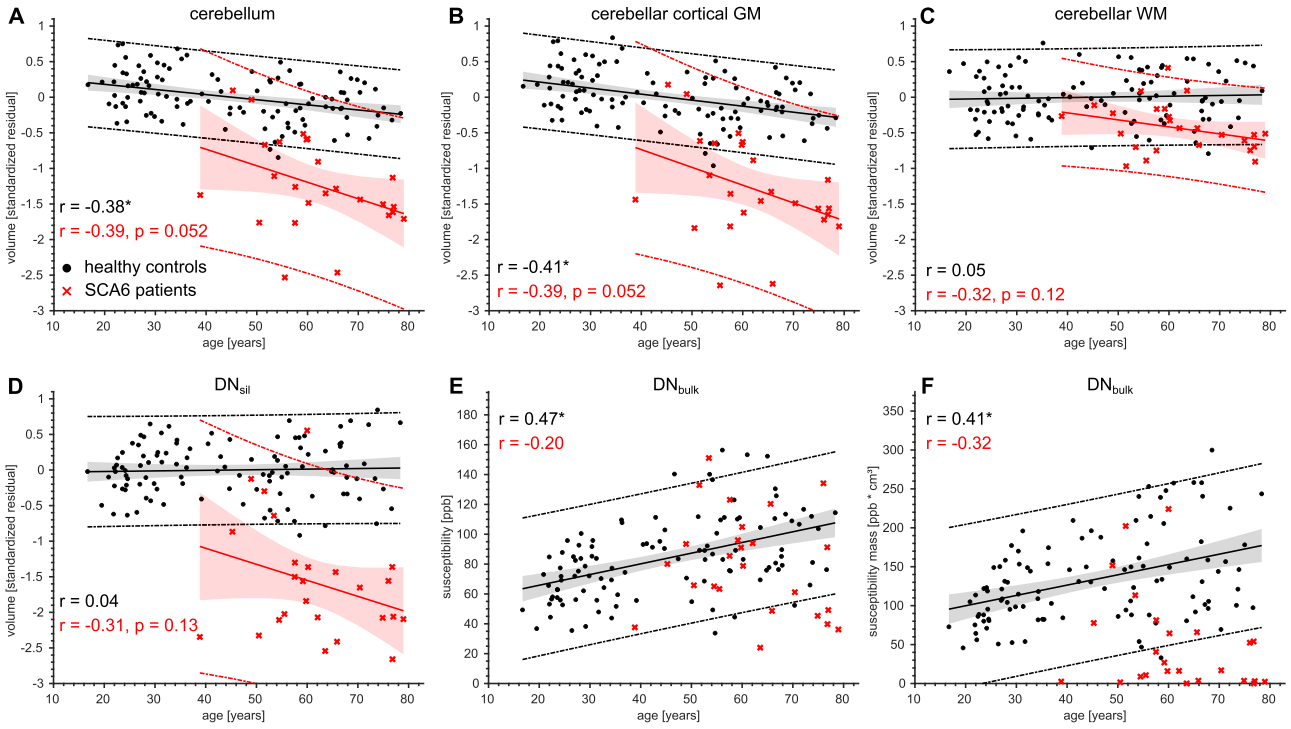

Fig. 3. Linear correlations of volume and susceptibility with respect to age in healthy controls and the SCA6 patients. The volumes (standardized residuals of total intracranial volume (TIV) corrected volumes) of the whole cerebellum, the cerebellar cortical gray matter, cerebellar white matter and dentate (DN_{sil}) are presented as functions of age in A-D, respectively. The relationship between magnetic susceptibility and susceptibility mass of DN_{bulk} with age is shown in E and F, respectively. The dots and crosses indicate the parameters measured in healthy controls and SCA6 patients, respectively. The solid line indicates the regression line. The 95% confidence interval and the 95% percent prediction interval are illustrated as shaded area and dashed line, respectively. The black color indicates elements related to the healthy controls, whereas the red elements are associated with the SCA6 patients. While not statistically significant, the regression line, confidence interval and prediction interval are also plotted for the volumes of DN_{sil} and WM in healthy controls to visually highlight the absence of correlation. r - Pearson's correlation coefficient. * – uncorrected *p*-value < 0.05. DN_{sil} – volume-of-interest reflecting the silhouette of the dentate nucleus. DN_{bulk} – volume-of-interest reflecting the bulk of iron-rich region of the dentate nucleus. ppb – parts-per-billion.

(VBM), Hulst et al. (2015) reported significant volume declines with age in lobules I-VII, Vermis Crus I, Vermis VIIb, lobules VIIIb, IX and X. Age-related decline of cerebellar volume has been described to be particularly prominent after the age of 70 years (Torvik et al., 1986). One explanation why we did not see significant age relationships for lobules IX and X is that our sample included only few subjects above 70 years (nine subjects with an age range from 70 to 78 years). Different to previous reports (Dimitrova et al., 2008; Hoogendam et al., 2012; Jernigan et al., 2001), we could not find a significant reduction of cerebellar white matter for healthy controls with increasing age. The reason might be different definitions of cerebellar white matter. In the present study, only the corpus medullare (i.e., the central white matter without the cerebellar nuclei) was defined as cerebellar white matter, whereas the other studies also added white matter areas that branch more deeply into the folia and the area of the cerebellar nuclei.

In addition, we found a tendency of linear relationships of the cerebellar cortex (uncorrected $p = 0.052$) and the whole cerebellar volumes (uncorrected $p < 0.052$) with age in the SCA6 patients (Supplementary Table 4). Interestingly, the slopes observed for the SCA6 cohort appeared to be steeper than the ones calculated for the healthy controls indicating faster age-related tissue decline in SCA6 patients, although the difference did not reach significance (Table 2). This finding is further supported by Schmitz-Hubsch et al. (2008a) who reported that only age at onset and disease duration determine disease-related symptoms as detected with the SARA score.

Regarding the dentate nuclei we observed that their size remained relatively stable across the lifespan of healthy subjects. This observation coincides with findings for the extent of the main body of the dentate nucleus ("dentate bulk") by He et al. (2017). Compared to He et al. (2017), we assessed the dentate volume more accurately and across a larger cohort with a broader range of age. Furthermore, we could not replicate the results of the histological post mortem study by Höpker (1951) who stated a loss of dentate volume at higher age. This discrepancy could be due to a relatively low number of subjects that were examined by Höpker and the histological techniques which do not reflect today's state-of-the-art. Maybe most importantly, histological shrinkage was mainly seen in an age group above 70 years, which made up only a small part of our investigated study population. One may argue, however, that the dentate nuclei may be easier to delineate in people with higher age because iron content increases with age (Lorio et al., 2014). This may have concealed small age-related decline in volume.

In line with previous literature (Acosta-Cabronero et al., 2016; Ghassaban et al., 2018; Li et al., 2014; Persson et al., 2015), we found a strong relationship of susceptibility with age for the main body of the dentate. The origin of the susceptibility-age relationship is the changing iron concentration within the dentate during lifespan. This is supported by findings of Hallgren and Sourander (1958), who histochemically observed that iron values within the dentate increase rapidly during the first two decades, and Ramos et al. (2014) who measured slightly lower amounts of iron for a subject group between 53 and 59 years ([244 ± 135] μg/g dry weight) than for subject groups larger than 60 years (about 290 μg/g dry weight).

The volumes of the dentate nuclei were more sensitive to differentiate between SCA6 and controls (Cohen's $d = 3.02$) compared to the volumes of the cerebellar cortex ($d = 2.04$) for reasons currently unknown. Fig. 3C demonstrates that the majority of SCA6 patients exhibit dentate nuclei volumes outside of the 95% prediction interval of the healthy controls. In four patients, however, the nuclei volumes were

Table 3
Absolute volumes and surfaces of the cerebellar nuclei determined based on susceptibility maps recorded at 3T and 7T are presented for all healthy controls, healthy controls age- and sex-matched to the SCA6 patients and SCA6 patients.

		3T			7T			histology[1]
Cohort		HC (all)	HC (SCA6)	SCA6	HC	HC (SCA6)	SCA6	HC
n		109	25	25	45	14	14	10
volume [cm³]								
cerebellum		139.3 ± 13.1 [136.8, 141.8]	139.0 ± 13.6* [133.4, 144.6]	105.8 ± 22.0* [96.7, 114.8]				
cerebellar GM[2]		127.5 ± 12.1 [125.2, 130.0]	126.7 ± 12.5* [121.5, 131.8]	95.4 ± 20.9* [86.8, 104.1]				
cerebellar cortex[3]		119.8 ± 11.6 [117.6, 122.0]	118.8 ± 12.1* [113.8, 123.8]	90.3 ± 19.8* [82.1, 98.4]				
white matter		11.8 ± 1.6 [11.5, 12.1]	12.3 ± 1.4* [11.7, 12.9]	10.3 ± 1.5* [9.7, 10.9]				
TIV		1523.1 ± 142 [1496.4, 1550.2]	1562±153 [1499, 1625]	1543±186 [1466, 1620]				
volume [mm³]								
DN_{sil}	left	333.8 ± 49# [324.6, 343.1]	350.8 ± 55*,# [328.1, 373.5]	149.1 ± 101* [107.4, 190.7]	265.7 ± 48# [251.1, 280.2]	261.0 ± 41*,# [237.5, 284.4]	125.0 ± 65* [87.5, 163]	394.5 ± 95
	right	328.1 ± 47# [319.2, 337.0]	340.4 ± 46*,# [321.3, 359.5]	142.5 ± 99* [101.6, 183.4]	269.8 ± 48# [255.4, 284.3]	260.0 ± 45*,# [234.1, 286.0]	119.2 ± 60* [84.3, 154.1]	390.2 ± 99
	sum	661.9 ± 92# [644.3, 679.4]	691.2 ± 98*,# [650.9, 731.6]	291.6 ± 199* [209.2, 373.9]	535.5 ± 93# [507.7, 563.3]	521.0 ± 83*,# [473.3, 568.7]	244.2 ± 125* [172.2, 316.3]	784.7 ± 193
DN_{bulk}	left	785.2 ± 170 [753.2, 817.6]	840.1 ± 176* [767.5, 912.6]	239.1 ± 273* [126.2, 352.0]	816.3 ± 220 [749.9, 882.6]	805.7 ± 214* [682.0, 929.4]	257.9 ± 231* [124.4, 391.4]	
	right	774.6 ± 172 [741.9, 807.2]	798.2 ± 156* [734.0, 862.4]	244.1 ± 294* [122.8, 365]	833.0 ± 245.7 [759.2, 906.9]	804.4 ± 181.3* [699.7, 909.1]	272.4 ± 248* [129.3, 415.6]	
	sum	1560.0 ± 330 [1497.3, 1622.6]	1638.3 ± 319* [1506.7, 1769.9]	483.2 ± 563* [250.9, 715.6]	1649.3 ± 411.5 [1525.7, 1772.9]	1610.1 ± 389* [1385.5, 1834.6]	530.3 ± 466* [261.4, 799.2]	
surface [mm²]								
DN_{sil}	left	1040.3 ± 136 [1014.5, 1066.1]	1085.2 ± 148* [1024.2, 1146.2]	467.2 ± 313* [338.1, 596.2]	1064.6 ± 182 [1009.9, 1119.3]	1056.6 ± 153* [968.5, 1144.7]	515.1 ± 263* [363.1, 667.1]	
	right	1018.3 ± 132 [993.3, 1043.3]	1046.6 ± 125* [994.9, 1098.4]	445.8 ± 309* [318.4, 573.2]	1069.9 ± 178 [1016.5, 1123.3]	1037.9 ± 159* [946.1, 1129.7]	491.4 ± 252* [345.7, 637.0]	
	mean	1029.3 ± 130.1 [1004.6, 1054.0]	1065.9.0 ± 133* [1011.2, 1120.6]	456.4 ± 310* [328.7, 584.3]	1067.3 ± 173 [1015.2, 1119.3]	1047.2 ± 151* [959.7, 1134.7]	503.2 ± 256* [355.2, 651.3]	

Values are presented as mean ± standard deviation. The 95% confidence interval is given in squared brackets. HC (all) – all control subjects. HC (SCA6) – control subjects matched to SCA6 patients. SCA6 – SCA6 patients. Differences between 3T and 7T as well as SCA and matched controls were probed using ANCOVA between the respective groups and age as covariate (Bonferroni-Holm correction accounting for multiple statistical tests (3T SCA6 vs. HC (SCA6): 14 tests; 3T vs. 7T: 9 tests). # indicates statistical significance between measures obtained at 3T and 7T. * indicates statistical significance between SCA6 patients and matched healthy controls. TIV – total intracranial volume. [1] – histological volumes of healthy controls determined via light microscopy of cell body stains published in Tellmann et al. (2015). [2] - volume of the whole GM including vermis and cerebellar nuclei. [3] – volume of the cerebellar GM excluding the vermis. DN_{sil} – volume-of-interest reflecting the silhouette of the dentate nucleus. DN_{bulk} – volume-of-interest reflecting the bulk of iron-rich region of the dentate nucleus. The cerebellar volume, the sum of the dentate across the two hemispheres and the TIV of SCA6 patients and their matched controls obtained at 3T without compensation for gradient-nonlinearity have already been published in Deistung et al., 2022.

within the prediction interval of the controls. One of these four patients was presymptomatic, whereas the remaining three patients were symptomatic and showed signs of ataxia (SARA scores: patient 3 = 4, patient 4 = 2, patient 5 = 9.5). Thus, although a reduced dentate volume allows identifying symptomatic patients with a high sensitivity, it does not appear to be an early marker of the disease. The latter, however, has to be confirmed in a larger group of presymptomatic patients.

Abnormal iron accumulation plays an important role in many neurodegenerative disorders, including Huntington's, Parkinson's, and Alzheimer's disease, and in multiple sclerosis (Moller et al., 2019; Zecca et al., 2004), but likely also contributes to cognitive decline in normal aging (Daugherty and Raz, 2015). It will be of interest to investigate in the future whether iron content in the dentate nuclei in the elderly contributes to cognitive decline given the contribution of the dentate nuclei to cognitive function (Dum and Strick, 2003; Thurling et al., 2012). There is evidence that in adulthood an increased iron content in deep gray matter structures such as the basal ganglia or the hypothalamus is associated with a decrease in cognitive abilities (Spence et al., 2020). Nevertheless, it has to be taken into account that the influence of iron should be considered as a complex homeostasis. For example, in adolescents a substandard concentration of iron in the basal ganglia is associated with a cognitive performance below average (Larsen et al., 2020). On the other hand, especially for the dentate nucleus there are hints that a lower iron content might be associated with a better working memory (Peterson et al., 2019). Probably a certain level of iron is crucial for the normal function of neuronal structures whereas either pathological or age-related accumulation leads to a decline in cerebral functions. The role of the iron content in the dentate nucleus and its possible influence on cognition remain unclear and need further investigation.

As discussed in more detail below, these findings likely reflect age-related alterations in glia but not in neurons.

4.2. SCA6 vs. healthy controls

Our cerebellar volumes observed in SCA6 patients and controls are in excellent agreement with previous MRI reports (Eichler et al., 2011; Schulz et al., 2010) and reflect a severe cerebellar tissue decline by about 25% in SCA6 patients. Our volume reductions observed in the cerebellar lobules and vermis in SCA6 patients are in line with previous reports

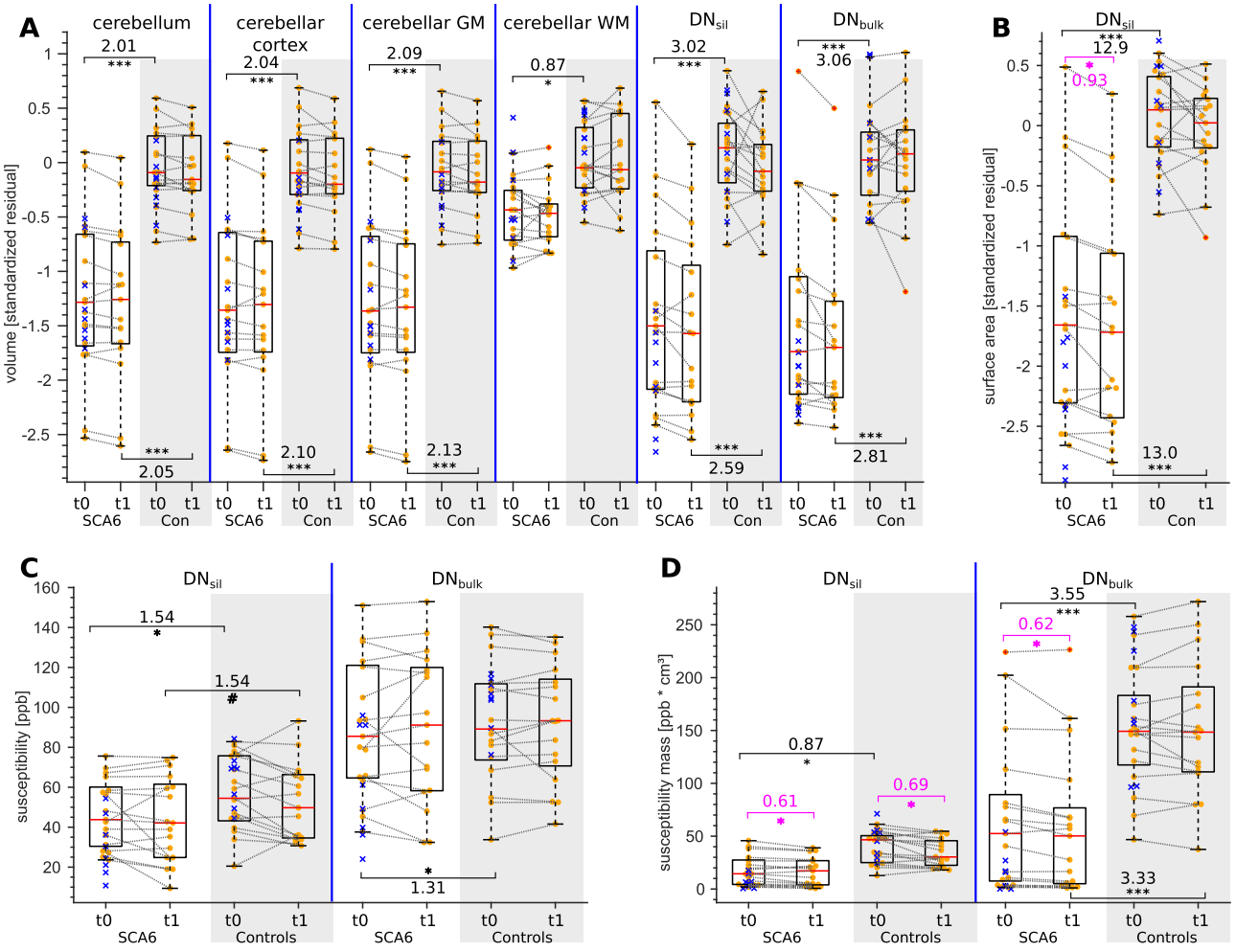

Fig. 4. Boxplots of volumes, surface area, susceptibility and susceptibility mass of cerebellar structures of SCA6 patients (white background) and their age- and sex-matched healthy controls (gray background). The measured values were derived from 3T-MRI data acquired at baseline (t_0) and 1 year follow-up (t_1). The volumes of the cerebellum, cerebellar cortex (without vermis), cerebellar GM (including vermis and cerebellar nuclei), cerebellar WM, DN_{sil} and DN_{bulk} are plotted in A. Normalized surface areas of DN_{sil} are displayed in B. Measurements of susceptibility and susceptibility mass of DN_{sil} and DN_{bulk} are plotted in C and D, respectively. Volumes (sum across both hemispheres) are presented as standardized residuals. Susceptibility masses are given as sum across both hemispheres, whereas susceptibilities and the normalized surface area are given as mean across both hemispheres. In each box, the solid red line indicates the median, and the bottom and top edges of the box indicate the 25th and 75th percentiles, respectively. The box and its whiskers are defined only by persons that received baseline and follow-up measurements (n=17). The solid orange dots indicate individual measurements of persons that received baseline and follow-up MRI ($n = 17$), whereas the blue x-symbols indicate persons that obtained only the baseline MRI ($n = 8$). Measurements at baseline (t_0) and follow-up (t_1) of the same subjects are connected via gray dashed lines. Statistical significant differences between SCA6 patients and controls obtained by linear mixed effects modeling are indicated by black asterisks (* - $p < 0.05$, ** - $p < 0.01$, *** - $p < 0.001$; Bonferroni-Holm correction for volumes: 19 different cerebellar regional volumes [DN_{sil}, DN_{bulk}, whole cerebellum, cerebellar GM and WM, lobules, vermis], Bonferroni-Holm correction for susceptibility or susceptibility mass: 2 comparisons for DN_{sil} and DN_{bulk}). Statistical significant differences between baseline and follow-up measurements assessed with paired *t*-test controlled for multiple hypothesis testing are indicated in purple (* - $p < 0.05$). Cohen's d is specified if statistical significance was present. SCA6 – SCA6 patients. Con – healthy controls matched to SCA6 patients. t_0 – baseline measurement. t_1 – follow-up measurement. DN_{sil} – volume-of-interest reflecting the silhouette of the dentate nucleus. DN_{bulk} – volume-of-interest reflecting the bulk of iron-rich region of the dentate nucleus. ppb – parts-per-billion. The cerebellar volume as well as the volume, susceptibility and susceptibility mass of the dentate nuclei obtained at baseline without correction for gradient-nonlinearity have already been published in Deistung et al., 2022.

relying on manual (Jung et al., 2012) and automatic volume segmentations (Yang et al., 2016) as well as VBM (Lukas et al., 2006; Schulz et al., 2010). In contrast to previous VBM studies, we also observed a significant decrease of white matter volume in SCA6 patients compared to controls. Reduced white matter volumes in SCA6 have also been reported in another volume-of-interest based analysis of structural T1w images (Yang et al., 2016) and is also supported by tissue decline of the superior and middle cerebellar peduncles as measured with diffusion tensor tractography (Falcon et al., 2016).

Data of dentate volume loss at 3T in SCA6 patients have already been partly reported (Deistung et al., 2022). The significantly reduced dentate volumes in the SCA6 group compared to matched controls confirm data of a recent 7T MRI study (Stefanescu et al., 2015). They are also in line with previous histological findings, which suggest an involvement of the cerebellar nuclei in SCA6 (Gierga et al., 2009; Wang et al., 2010).

SCA6 is a form of more pure cerebellar degeneration, which primarily results in degeneration of the Purkinje cells. In transgenic mouse models, Triarhou et al. (1987) and Sultan et al. (2002) showed that a loss of Purkinje cell input led to a loss of volume in the cerebellar nuclei that could not be explained by the loss of dentate neurons. In fact, investigations by Heckroth (1994) revealed that the reduction of nuclei volume is mainly driven by the loss of myelinated axons and synapses with a proportion of more than 50%. About one third of dentate volume loss was due to glial processes, vessels and intercellular space,

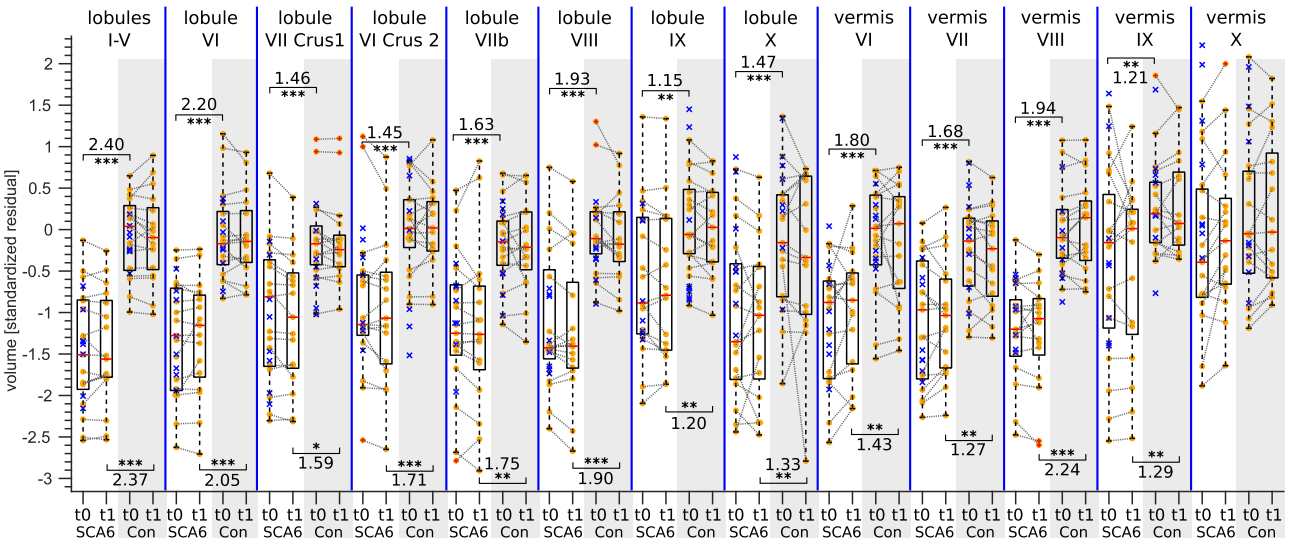

Fig. 5. Boxplots of volumes of the individual cerebellar lobules of SCA6 patients (white background) and matched healthy controls (gray background). The volumes were derived from 3T-MRI data acquired at baseline (t_0) and 1 year follow-up (t_1). Volumes (sum across both hemispheres) are presented as standardized residuals. In each box, the solid red line indicates the median, and the bottom and top edges of the box indicate the 25th and 75th percentiles, respectively. The box and its whiskers are defined only by persons that received baseline and follow-up measurements (n = 17). The solid orange dots indicate individual measurements of persons that received baseline and follow-up MRI (n = 17), whereas the blue x-symbols indicate persons that obtained only the baseline MRI (n = 8). Measurements at baseline (t_0) and follow-up (t_1) of the same subjects are connected via gray dashed lines. Statistical significant differences between SCA6 patients and controls obtained by linear mixed effects modeling are indicated by black asterisks (* - $p < 0.05$, ** - $p < 0.01$, *** - $p < 0.001$, Bonferroni-Holm correction accounting for the statistical tests of 19 different cerebellar regional volumes [DN_{sil}, DN_{bulk}, whole cerebellum, cerebellar GM and WM, lobules, vermis]). Paired t-tests controlled for multiple hypothesis testing did not yield statistically significant differences between baseline and follow-up. Cohen's d is specified if statistical significance was present. SCA6 – SCA6 patients. Con – healthy controls matched to SCA6 patients. t_0 – baseline measurement. t_1 – follow-up measurement.

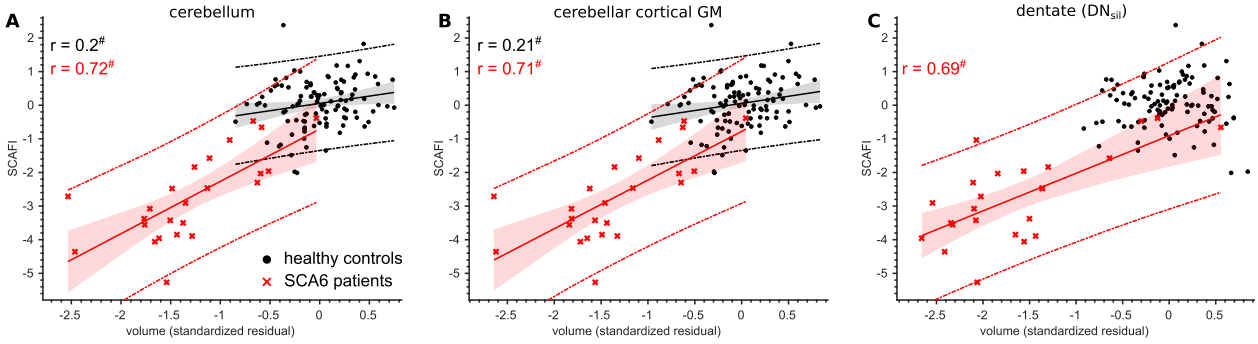

Fig. 6. Linear correlations of SCAFI scores with respect to volumes of selected structures for both healthy controls and the SCA6 patients. Correlations are presented as functions of normalized volumes of the whole cerebellum, the cerebellar cortical gray matter (without vermis) as well as the outlined dentate nuclei (DN_{sil}). The black dots and red crosses indicate the parameters measured in healthy controls and SCA6 patients, respectively. The 95% confidence interval and the 95% prediction interval are illustrated as shaded area and dashed line, respectively. r - Pearson's correlation coefficient. # – uncorrected p-value < 0.05.

whereas only a minor proportion could be accounted to the depletion of neurons.

We measured significantly reduced susceptibilities and susceptibility masses in the gray matter rim of the dentate wall (DN_{sil}) and in the body of the dentate (DN_{bulk}) in the group of all SCA6 patients compared to healthy controls at baseline (Fig. 4). These findings suggest a depletion of iron in the dentate nuclei of the patients. The results of reduced susceptibility in the dentate nucleus in patients with SCA6 are consistent with previous findings (Deistung et al., 2022; Sugiyama et al., 2019). Of note, studies in rats have shown that iron in the cerebellum and its nuclei is primarily stored in oligodendrocytes and microglia (Benkovic and Connor, 1993). Thus, our findings suggest that the decreased nuclei size does not reflect a decrease in the number of neurons. Rather it may reflect a decrease of oligodendrocytes and/or microglia – which is exactly what one would expect based on the findings in transgenic mouse models (Heckroth, 1994; Sultan et al., 2002; Triarhou et al., 1987). As yet, glia cell involvement has not yet been studied in SCA6.

It is commonly assumed that the Purkinje cell loss is the primary deficit in SCA6 (Falcon et al., 2016; Gomez et al., 1997). In that case, the assumed reduction of the oligodendroglia would be secondary. However, it cannot be excluded that oligodendroglia are primarily involved. This assumption is supported by neuropathological findings in transgenic MBP-TK mice. Here, selective ablation of oligodendrocytes during the first weeks of postnatal life resulted in disruption of the cortical cytoarchitecture and neuronal network (Collin et al., 2007; Mathis et al., 2003), resembling histological findings in human SCA6 brains (Gierga et al., 2009; Yang et al., 2000).

Of note, the lower susceptibility values measured in patients may not only be influenced by alterations in iron but also by myelin degradation (Liu et al., 2011). Furthermore, one may argue that microcalcifications, which would result in a decrease of susceptibility values, may play a role, but this has not been studied in SCA6 patients. Further histological studies are needed to understand the reasons for the lower susceptibility in SCA6.

4.3. Longitudinal investigation

Linear mixed effects modeling did not suggest a change in a volume measure (cerebellar lobes, WM, dentate nucleus) after 1 year follow-up when investigating the normalized volumes within one model for patients and controls, respectively. As the linear mixed model was sensitive to group-based differences, paired t-tests have also been applied to investigate changes between baseline and follow-up. Taking into account multiple comparisons no volume measure differed significantly at follow-up. The observation period of one year was likely too short and the control and patient populations available for follow-up to small. Within a longer observation interval of 3.7 years (±1.9 years, range: 1–9 years)) and a substantially higher number of healthy controls (n = 537), Han et al. (2020) detected longitudinal volume decreases in the whole cerebellum, corpus medullare and in the majority of the cerebellar lobules but not in vermis VII, VIII, and X, the left anterior lobe, as well as the right lobes VIIIA and X. Adanyeguh et al. (2018) did not detect cerebellar and pontine volume changes in healthy controls ($n = 24$; age: 50 $y \pm 13$ y [26–67]) after two years but statistical significant reductions in the pons and cerebellum in SCA1, SCA2, SCA3 and SCA7. Reetz et al. (2013) evaluated the changes of volumes in patients with SCA1, SCA3 and SCA6 over a two-year interval. They did not observe statistical significant differences in the volumes of the cerebellum (baseline: 5.87% ± 1.01%, follow-up: 5.78% ± 0.77% [volumes are given as a percentage of the TIV]) and vermis (baseline: 0.88% ± 0.32%, follow-up: 0.85% ± 0.31%) in SCA6. Compared to SCA1 and SCA3 patients, SCA6 patients showed pronounced volume loss in the mesencephalon and cerebrum within the 2-year observation interval. We did not observe changes in dentate susceptibility after 1 year. In Friedreich ataxia higher susceptibility has been reported with an increase of 8.4 ppb/year and 6.7ppb/year in the left and right DN_{bulk}, respectively, after two years, whereas the DN_{bulk} susceptibility of the control group did not substantially differ over time (Ward et al., 2019). We found lower susceptibility masses and dentate surfaces at follow-up for SCA6 patients, however, more research is required to establish this finding in a larger cohort. Longitudinal studies with longer observation intervals and higher number of subjects are needed to reliably show age- and disease-related decline.

Natural history studies show that the annual SARA score increase in SCA6 is small compared to other SCAs. In their seminal study, Jacobi et al. (2015) report an annual SARA score increase of 2.11 (SE = 0.12) in patients with SCA1, 1.49 (SE = 0.07) in patients with SCA2, and 1.56 (SE = 0.08) in patients with SCA3, but only 0.80 (SE = 0.09) in patients with SCA6. These findings were largely confirmed in a recent meta-analysis of six longitudinal natural history studies of SCA patients (Diallo et al., 2021). The authors report an annual pooled SARA score of 1.83 (1.46–2.20) in patients with SCA1, 1.40 (1.19–1.61) in patients with SCA2, and 1.41 (0.97–1.84) in patients with SCA3, but only 0.81 (0.66–0.97) in patients with SCA6. The annual SARA score increase (0.44 and 0.95) observed in the present study is in good agreement.

4.4. Assessment of dentate nuclei

We were able to reliably identify the dentate nuclei on quantitative susceptibility maps acquired at 3T and 7T. Parameters extracted from the manual demarcations were highly consistent between and within the raters (see Supplementary Section 2).

While some MRI studies determined the dentate vbzcolume based on the extent of the main body of the dentate nucleus (i.e., nuclei's gray matter rim including the enclosed white matter) (Dimitrova et al., 2006; He et al., 2017), we also assessed the nuclei volume based on its corrugated thin walls, in line with histological observations (Stilling, 1878; Tellmann et al., 2015; Voogd and Ruigrok, 2012). Our dentate volumes in healthy subjects are well within the range reported in the histological literature. While Höpker (1951) determined an average dentate volume of 315.7 mm^3 (27 subjects; age: 6–99 years), Tellmann et al. (2015), using up-to-date histological techniques, reported 784.7 ± 193 mm^3 (10 subjects; age: 30–85 years). For comparison, Diedrichsen et al. (2011) and Stefanescu et al. (2015) reported average dentate volumes of 729 mm^3 (23 subjects, age: 21–61 years) and 400.2 mm^3 (23 subjects, age: 22–75 years, individual volume (200.1 ± 89.3) mm^3) by analyzing 0.5 mm isotropic 7T-MRI images. Assuming the dentate volume from Tellmann et al. (2015) as ground truth, the volume was most accurately mapped by Diedrichsen et al. (2011) using SWI phase images at 7T, followed by our own 3T and 7T QSM measurements (Table 3) and by Stefanescu et al. (2015) relying on SWI images at 7T. The highest accuracy of the dentate volume measured on phase images instead on susceptibility maps compared to the histologically observed volume by Tellmann et al. (2015) seems to be unexpected at first. QSM should provide a more accurate depiction of the dentate and our resolution of 0.38 mm at 7T was even 24% higher than the one used by Diedrichsen et al. (2011). As QSM is expected to be more accurate in anatomically delineating iron stores compared to phase or SWI images (Deistung et al., 2013, 2017, 2016; Ghassaban et al., 2018), a possible explanation for our lower volumes could be attributed to an inhomogeneous iron distribution within the dentate nucleus. From histology it is known that the ventromedial portion of the dentate nucleus exhibits less amounts of iron compared to the dorsolateral part (Gans, 1924; Höpker, 1951; Jansen et al., 1958). As a consequence, some parts of the nuclei area might be only barely seen or even invisible on QSM, whereas due to the non-locality of the phase (Schäfer et al., 2009) the remaining structures gathered with phase images are overestimated.

Dentate volumes at 7T (DN_{sil}, healthy controls, 535.5 ± 93 mm^3) were smaller than at 3T (DN_{sil}, healthy controls, 661.9 ± 92 mm^3). This is most likely explained by different spatial imaging resolutions. Of note, voxel volume at 7T was 56% smaller than at 3T. Thus, the contribution of partial volume effects was markedly reduced at 7T. In fact, the surfaces of the dentate nuclei were approximately 4% larger at 7T than at 3T (Table 3) indicating that the folding pattern of the dentate nuclei could be more accurately traced at 7T. In addition, we did not observe statistical significances of the dentate surfaces when comparing exactly the same cohort at 3T and 7T (see Supplementary Section S4). Thus, the surface is more robust against different image resolutions than the volume measure. Further statistical analysis results when comparing 3T and 7T outcome measures are provided in Supplementary Section S4.

4.5. Limitations

There are four main limitations. Firstly, QSM has turned out to be a valid method to assess the volume of the dentate nuclei even at the conventional field strength of 3T. However, QSM was unable to display the corrugated wall of the dentate nuclei with an accuracy that comes close to histology. This is because QSM likely does not show the extent of the dentate neurons, but rather the distribution of the iron-containing glia cells (as discussed above). As a consequence, QSM shows more than the thin wall of the dentate nucleus, and the white matter inside the nucleus is also visible (see e.g. Fig. 1). If one goes back to the early iron stainings by Gans (1924), a similar distribution of iron positive cells can already be seen. Secondly, high iron concentration has been shown to bias estimates of regional volumes including volumes of the dentate nuclei using automatic parcellations (Lorio et al., 2014). Although, in the present study the gold standard, that is manual delineation of the dentate nuclei has been used, it cannot be excluded that increased iron content led to better visibility on QSM maps, and therefore biased manual delineation.

Thirdly, we like to note that although Stefanescu et al. (2015) showed significantly smaller nuclei in SCA6 compared to controls (very similar to our study), the absolute volumes for the dentate nuclei were significantly smaller compared to the present study, presumably because of different strategies in manual delineation of the nuclei. Therefore, automated strategies for delineation of the cerebellar nuclei are needed to achieve improved reproducibility and, thus, comparability among different studies.

Fourthly, a subset (18%) of the control group was scanned on a different MRI system, and in particular, using a much more advanced head coil. These data were only considered in investigations of age-related effects and correlations with SCAFI. To rule out a potential bias due to the MRI scanner, we compiled a similarly aged cohort scanned at the other site (age site 1: 28.4 ± 4.6 years; age site 2: 27.0 ± 3.4 years) and ran two-sampled t-tests between each metric for each site in order to identify potential statistical significances. Within these cohorts, neither age nor volumes and susceptibilities exhibited statistically significance between the two sites indicating that pooling the observed metrics does not bias the outcome of the analyzes. The volumes and susceptibilities for these cohorts are summarized in Supplementary Fig. 5.

5. Conclusions

QSM enabled us to assess the dentate nuclei already at a magnetic field strength of 3 Tesla, which is widely used in clinical settings. Volume measures of the dentate nuclei were in good accordance with histological data. In contrast to the well-known age-dependent decline of cerebellar GM, the volume of the dentate nuclei assessed by QSM did not depend on age, at least in the age range of 18 and 78 years, whereas its iron load increased during lifespan. Previous findings of markedly reduced volumes of the cerebellar lobules and dentate nuclei in SCA6 at 7 Tesla were confirmed at 3 Tesla. No significant changes in the volumes of the cerebellar lobules and dentate nuclei were observed in a one year follow-up in SCA6 patients and controls limiting their value as a biomarker.

Funding

The study was funded by the German Research Foundation (DFG, DE 2516/1-1 and TI 239/17-1) and the Else Kröner-Fresenius-Stiftung (Essener Ausbildungsprogramm "Labor und Wissenschaft" für den ärztlichen Nachwuchs, ELAN, awarded to D. Jäschke).

Declaration of Competing Interest

The authors report no applicable competing interests pertaining to this publication. There are no products used or discussed within our study.

Credit authorship contribution statement

Dominik Jäschke: Conceptualization, Formal analysis, Investigation, Writing – original draft, Writing – review & editing, Visualization. **Katharina M. Steiner:** Investigation, Writing – review & editing. **Dae-In Chang:** Investigation, Writing – review & editing. **Jens Claaßen:** Investigation, Writing – review & editing. **Ellen Uslar:** Investigation, Writing – review & editing. **Andreas Thieme:** Investigation, Writing – review & editing. **Marcus Gerwig:** Investigation, Writing – review & editing. **Viktor Pfaffenrot:** Investigation, Writing – review & editing. **Thomas Hulst:** Investigation, Writing – review & editing. **Alexander Gussew:** Investigation, Writing – review & editing. **Stefan Maderwald:** Investigation, Writing – review & editing. **Sophia L. Göricke:** Investigation, Writing – review & editing. **Martina Minnerop:** Investigation, Writing – review & editing. **Mark E. Ladd:** Investigation, Writing – review & editing. **Jürgen R. Reichenbach:** Conceptualization, Resources, Writing – review & editing. **Dagmar Timmann:** Conceptualization, Investigation, Project administration, Funding acquisition, Writing – original draft, Writing – review & editing. **Andreas Deistung:** Conceptualization, Methodology, Software, Formal analysis, Investigation, Writing – original draft, Writing – review & editing, Visualization, Project administration, Funding acquisition.

Acknowledgments

We thank Beate Brol (Department of Neurology and Center for Translational Neuro- and Behavioral Sciences (C-TNBS), Essen University Hospital, Germany) for manual delineation of the deep cerebellar nuclei and Dr. Franziska Labrenz (Department of Neurology and Center for Translational Neuro- and Behavioral Sciences (C-TNBS), Essen University Hospital, Germany) for statistical advices. We are also grateful to Dr. Danial Gallichan (Cardiff University Brain Research Imaging Centre (CUBRIC), School of Engineering, Cardiff University, United Kingdom) and Dr. José P. Marques (Donders Insitute for Brain, Cognition and Behavior, Radbound University Nijmegen, The Netherlands) for sharing their gradient-echo sequence with fat-navigators and assistance in gradient-echo raw data reconstruction. We thank Dr. Simon Hametner (Department of Neuroimmunology, Medical University of Vienna, Austria) for valuable discussions about iron storage in the brain as well as Dr. Oliver Kraff (Erwin L. Hahn Institute for Magnetic Resonance Imaging, University of Duisburg-Essen, Essen, Germany) for support in solving MRI safety issues.

Supplementary materials

Supplementary material associated with this article can be found, in the online version, at doi:10.1016/j.neuroimage.2023.119950.

References

Acosta-Cabronero, J., Betts, M.J., Cardenas-Blanco, A., Yang, S., Nestor, P.J., 2016. *In vivo* MRI mapping of brain iron deposition across the adult lifespan. J. Neurosci. 36, 364–374.

Adanyeguh, I.M., Perlbarg, V., Henry, P.G., Rinaldi, D., Petit, E., Valabregue, R., Brice, A., Durr, A., Mochel, F., 2018. Autosomal dominant cerebellar ataxias: imaging biomarkers with high effect sizes. NeuroImage Clin. 19, 858–867.

Andersen, B.B., Gundersen, H.J., Pakkenberg, B., 2003. Aging of the human cerebellum: a stereological study. J. Comput. Neurol. 466, 356–365.

Aoki, S., Okada, Y., Nishimura, K., Barkovich, A.J., Kjos, B.O., Brasch, R.C., Norman, D., 1989. Normal deposition of brain iron in childhood and adolescence: MR imaging at 1.5 T. Radiology 172, 381–385.

Benkovic, S.A., Connor, J.R., 1993. Ferritin, transferrin, and iron in selected regions of the adult and aged rat brain. J. Comput. Neurol. 338, 97–113.

Bernard, J.A., Seidler, R.D., 2013. Relationships between regional cerebellar volume and sensorimotor and cognitive function in young and older adults. Cerebellum 12, 721–737.

Bernard, J.A., Seidler, R.D., 2014. Moving forward: age effects on the cerebellum underlie cognitive and motor declines. Neurosci. Biobehav. Rev. 42, 193–207.

Bilgic, B., Pfefferbaum, A., Rohlfing, T., Sullivan, E.V., Adalsteinsson, E., 2012. MRI estimates of brain iron concentration in normal aging using quantitative susceptibility mapping. NeuroImage 59, 2625–2635.

Collin, L., Doretto, S., Malerba, M., Ruat, M., Borrelli, E., 2007. Oligodendrocyte ablation affects the coordinated interaction between granule and Purkinje neurons during cerebellum development. Exp. Cell Res. 313, 2946–2957.

Daugherty, A.M., Raz, N., 2015. Appraising the role of iron in brain aging and cognition: promises and limitations of MRI methods. Neuropsychol. Rev. 25, 272–287.

Deistung, A., Jäschke, D., Draganova, R., Pfaffenrot, V., Hulst, T., Steiner, K.M., Thieme, A., Giordano, I.A., Klockgether, T., Tunc, S., Münchau, A., Minnerop, M., Göricke, S.L., Reichenbach, J.R., Timmann, D., 2022. Quantitative susceptibility mapping reveals alterations of dentate nuclei in common types of degenerative cerebellar ataxias. Brain Commun. 4(1):fcab306. doi:10.1093/braincomms/fcab306. eCollection 2022.

Deistung, A., Schäfer, A., Schweser, F., Biedermann, U., Turner, R., Reichenbach, J.R., 2013. Toward *in vivo* histology: a comparison of quantitative susceptibility mapping (QSM) with magnitude-, phase-, and R2*-imaging at ultra-high magnetic field strength. NeuroImage 65, 299–314.

Deistung, A., Schweser, F., Reichenbach, J.R., 2017. Overview of quantitative susceptibility mapping. NMR Biomed 30. doi:10.1002/nbm.3569.

Deistung, A., Stefanescu, M.R., Ernst, T.M., Schlamann, M., Ladd, M.E., Reichenbach, J.R., Timmann, D., 2016. Structural and functional magnetic resonance imaging of the cerebellum: considerations for assessing cerebellar ataxias. Cerebellum 15, 21–25.

Destrieux, C., Fischl, B., Dale, A., Halgren, E., 2010. Automatic parcellation of human cortical gyri and sulci using standard anatomical nomenclature. NeuroImage 53, 1–15.

Diallo, A., Jacobi, H., Tezenas du Montcel, S., Klockgether, T., 2021. Natural history of most common spinocerebellar ataxia: a systematic review and meta-analysis. J. Neurol. 268, 2749–2756.

Diedrichsen, J., 2006. A spatially unbiased atlas template of the human cerebellum. NeuroImage 33, 127–138.

Diedrichsen, J., Balsters, J.H., Flavell, J., Cussans, E., Ramnani, N., 2009. A probabilistic MR atlas of the human cerebellum. NeuroImage 46, 39–46.

Diedrichsen, J., Maderwald, S., Kuper, M., Thurling, M., Rabe, K., Gizewski, E.R., Ladd, M.E., Timmann, D., 2011. Imaging the deep cerebellar nuclei: a probabilistic atlas and normalization procedure. NeuroImage 54, 1786–1794.

Dimitrova, A., Gerwig, M., Brol, B., Gizewski, E.R., Forsting, M., Beck, A., Aurich, V., Kolb, F.P., Timmann, D., 2008. Correlation of cerebellar volume with eyeblink conditioning in healthy subjects and in patients with cerebellar cortical degeneration. Brain Res. 1198, 73–84.
Dimitrova, A., Zeljko, D., Schwarze, F., Maschke, M., Gerwig, M., Frings, M., Beck, A., Aurich, V., Forsting, M., Timmann, D., 2006. Probabilistic 3D MRI atlas of the human cerebellar dentate/interposed nuclei. Neuroimage 30, 12–25.
Drayer, B., Burger, P., Darwin, R., Riederer, S., Herfkens, R., Johnson, G.A., 1986. MRI of brain iron. AJR Am. J. Roentgenol. 147, 103–110.
Dum, R.P., Strick, P.L., 2003. An unfolded map of the cerebellar dentate nucleus and its projections to the cerebral cortex. J. Neurophysiol. 89, 634–639.
Eckstein, K., Dymerska, B., Bachrata, B., Bogner, W., Poljanc, K., Trattnig, S., Robinson, S.D., 2018. Computationally efficient combination of multi-channel phase data from multi-echo acquisitions (ASPIRE). Magn. Reson. Med. 79, 2996–3006.
Eichler, L., Bellenberg, B., Hahn, H.K., Koster, O., Schols, L., Lukas, C., 2011. Quantitative assessment of brain stem and cerebellar atrophy in spinocerebellar ataxia types 3 and 6: impact on clinical status. AJNR Am. J. Neuroradiol. 32, 890–897.
Falcon, M.I., Gomez, C.M., Chen, E.E., Shereen, A., Solodkin, A., 2016. Early cerebellar network shifting in spinocerebellar ataxia type 6. Cereb. Cortex 26, 3205–3218.
Fischl, B., Salat, D.H., Busa, E., Albert, M., Dieterich, M., Haselgrove, C., van der Kouwe, A., Killiany, R., Kennedy, D., Klaveness, S., Montillo, A., Makris, N., Rosen, B., Dale, A.M., 2002. Whole brain segmentation: automated labeling of neuroanatomical structures in the human brain. Neuron 33, 341–355.
Gallichan, D., Marques, J.P., Gruetter, R., 2016. Retrospective correction of involuntary microscopic head movement using highly accelerated fat image navigators (3D FatNavs) at 7T. Magn. Reson. Med. 75, 1030–1039.
Gans, A., 1924. Beitrag zur Kenntnis des Aufbaus des Nucleus Dentatus aus zwei Teilen, namentlich auf Grund von Untersuchungen mit der Eisenreaktion. Z. für die Gesamte Neurol. Psychiatr. 93, 750–755.
Ghassaban, K., Liu, S., Jiang, C., Haacke, E.M., 2018. Quantifying iron content in magnetic resonance imaging. NeuroImage 187, 77–92.
Gierga, K., Schelhaas, H.J., Brunt, E.R., Seidel, K., Scherzed, W., Egensperger, R., de Vos, R.A., den Dunnen, W., Ippel, P.F., Petrasch-Parwez, E., Deller, T., Schols, L., Rub, U., 2009. Spinocerebellar ataxia type 6 (SCA6): neurodegeneration goes beyond the known brain predilection sites. Neuropathol. Appl. Neurobiol. 35, 515–527.
Gomez, C.M., Thompson, R.M., Gammack, J.T., Perlman, S.L., Dobyns, W.B., Truwit, C.L., Zee, D.S., Clark, H.B., Anderson, J.H., 1997. Spinocerebellar ataxia type 6: gaze-evoked and vertical nystagmus, Purkinje cell degeneration, and variable age of onset. Ann. Neurol. 42, 933–950.
Haacke, E.M., Xu, Y., Cheng, Y.C., Reichenbach, J.R., 2004. Susceptibility weighted imaging (SWI). Magn. Reson. Med. 52, 612–618.
Hallgren, B., Sourander, P., 1958. The effect of age on the non-haemin iron in the human brain. J. Neurochem. 3, 41–51.
Hametner, S., Endmayr, V., Deistung, A., Palmrich, P., Prihoda, M., Haimburger, E., Menard, C., Feng, X., Haider, T., Leisser, M., Kock, U., Kaider, A., Hoftberger, R., Robinson, S., Reichenbach, J.R., Lassmann, H., Traxler, H., Trattnig, S., Grabner, G., 2018. The influence of brain iron and myelin on magnetic susceptibility and effective transverse relaxation - A biochemical and histological validation study. NeuroImage 179, 117–133.
Han, S., An, Y., Carass, A., Prince, J.L., Resnick, S.M., 2020. Longitudinal analysis of regional cerebellum volumes during normal aging. NeuroImage 220, 117062.
He, N., Langley, J., Huddleston, D.E., Ling, H., Xu, H., Liu, C., Yan, F., Hu, X.P., 2017. Improved neuroimaging atlas of the dentate nucleus. Cerebellum 16, 951–956.
Heckroth, J.A., 1994. A quantitative morphological analysis of the cerebellar nuclei in normal and lurcher mutant mice. II. Volumetric changes in cytological components. J. Comput. Neurol. 343, 183–192.
Hernandez-Torres, E., Wiggermann, V., Machan, L., Sadovnick, A.D., Li, D.K.B., Traboulsee, A., Hametner, S., Rauscher, A., 2018. Increased mean R2* in the deep gray matter of multiple sclerosis patients: have we been measuring atrophy? J. Magn. Reson. Imaging 50, 201–208.
Holm, S., 1979. A Simple Sequentially Rejective Multiple Test Procedure. Scand. J. Stat. 6, 65–70.
Hoogendam, Y.Y., van der Geest, J.N., van der Lijn, F., van der Lugt, A., Niessen, W.J., Krestin, G.P., Hofman, A., Vernooij, M.W., Breteler, M.M., Ikram, M.A., 2012. Determinants of cerebellar and cerebral volume in the general elderly population. Neurobiol. Aging 33, 2774–2781.
Höpker, W., 1951. Das Altern des Nucleus dentatus. Zschr. Alternsforsch. 5, 256–277.
Hulst, T., van der Geest, J.N., Thurling, M., Goericke, S., Frens, M.A., Timmann, D., Donchin, O., 2015. Ageing shows a pattern of cerebellar degeneration analogous, but not equal, to that in patients suffering from cerebellar degenerative disease. NeuroImage 116, 196–206.
Jacobi, H., du Montcel, S.T., Bauer, P., Giunti, P., Cook, A., Labrum, R., Parkinson, M.H., Durr, A., Brice, A., Charles, P., Marelli, C., Mariotti, C., Nanetti, L., Panzeri, M., Rakowicz, M., Sulek, A., Sobanska, A., Schmitz-Hubsch, T., Schols, L., Hengel, H., Baliko, L., Melegh, B., Filla, A., Antenora, A., Infante, J., Berciano, J., van de Warrenburg, B.P., Timmann, D., Szymanski, S., Boesch, S., Kang, J.S., Pandolfo, M., Schulz, J.B., Molho, S., Diallo, A., Klockgether, T., 2015. Long-term disease progression in spinocerebellar ataxia types 1, 2, 3, and 6: a longitudinal cohort study. Lancet Neurol. 14, 1101–1108.
v Jansen, J., Brodal, A., Bargmann, W., Möllendorff, W., Bargmann, W., 1958. Das Kleinhirn. In: Handbuch Der Mikroskopischen Anatomie des Menschen. Springer-Verlag, Berlin, Göttingen, Heidelberg, pp. 91–162.
Jernigan, T.L., Archibald, S.L., Fennema-Notestine, C., Gamst, A.C., Stout, J.C., Bonner, J., Hesselink, J.R., 2001. Effects of age on tissues and regions of the cerebrum and cerebellum. Neurobiol. Aging 22, 581–594.
Jung, B.C., Choi, S.I., Du, A.X., Cuzzocreo, J.L., Geng, Z.Z., Ying, H.S., Perlman, S.L., Toga, A.W., Prince, J.L., Ying, S.H., 2012. Principal component analysis of cerebellar shape on MRI separates SCA types 2 and 6 into two archetypal modes of degeneration. Cerebellum 11, 887–895.
Klockgether, T., 2011. Update on degenerative ataxias. Curr. Opin. Neurol. 24, 339–345.
Koeppen, A.H., 2005. The pathogenesis of spinocerebellar ataxia. Cerebellum 4, 62–73.
Koeppen, A.H., Ramirez, R.L., Yu, D., Collins, S.E., Qian, J., Parsons, P.J., Yang, K.X., Chen, Z., Mazurkiewicz, J.E., Feustel, P.J., 2012. Friedreich's ataxia causes redistribution of iron, copper, and zinc in the dentate nucleus. Cerebellum 11, 845–860.
Koppelmans, V., Hirsiger, S., Merillat, S., Jancke, L., Seidler, R.D., 2015. Cerebellar gray and white matter volume and their relation with age and manual motor performance in healthy older adults. Hum. Brain Mapp. 36, 2352–2363.
Langkammer, C., Schweser, F., Krebs, N., Deistung, A., Goessler, W., Scheurer, E., Sommer, K., Reishofer, G., Yen, K., Fazekas, F., Ropele, S., Reichenbach, J.R., 2012. Quantitative susceptibility mapping (QSM) as a means to measure brain iron? A post mortem validation study. NeuroImage 62, 1593–1599.
Larsen, B., Bourque, J., Moore, T.M., Adebimpe, A., Calkins, M.E., Elliott, M.A., Gur, R.C., Gur, R.E., Moberg, P.J., Roalf, D.R., Ruparel, K., Turetsky, B.I., Vandekar, S.N., Wolf, D.H., Shinohara, R.T., Satterthwaite, T.D., 2020. Longitudinal development of brain iron is linked to cognition in youth. J. Neurosci. 40, 1810–1818.
Legland, D., Kiêu, K., Devaux, M.F., 2007. Computation of Minkowski measures on 2D and 3D binary images. Image Anal. Stereol. 26, 83–92.
Li, S.C., Lindenberger, U., Sikstrom, S., 2001. Aging cognition: from neuromodulation to representation. Trends Cogn. Sci. 5, 479–486.
Li, W., Wang, N., Yu, F., Han, H., Cao, W., Romero, R., Tantiwongkosi, B., Duong, T.Q., Liu, C., 2015. A method for estimating and removing streaking artifacts in quantitative susceptibility mapping. NeuroImage 108, 111–122.
Li, W., Wu, B., Batrachenko, A., Bancroft-Wu, V., Morey, R.A., Shashi, V., Langkammer, C., De Bellis, M.D., Ropele, S., Song, A.W., Liu, C., 2014. Differential developmental trajectories of magnetic susceptibility in human brain gray and white matter over the lifespan. Hum. Brain Mapp. 35, 2698–2713.
Liu, C., Li, W., Johnson, G.A., Wu, B., 2011. High-field (9.4 T) MRI of brain dysmyelination by quantitative mapping of magnetic susceptibility. NeuroImage 56, 930–938.
Lorio, S., Lutti, A., Kherif, F., Ruef, A., Dukart, J., Chowdhury, R., Frackowiak, R.S., Ashburner, J., Helms, G., Weiskopf, N., Draganski, B., 2014. Disentangling *in vivo* the effects of iron content and atrophy on the ageing human brain. NeuroImage 103, 280–289.
Lukas, C., Schols, L., Bellenberg, B., Rub, U., Przuntek, H., Schmid, G., Koster, O., Suchan, B., 2006. Dissociation of grey and white matter reduction in spinocerebellar ataxia type 3 and 6: a voxel-based morphometry study. Neurosci. Lett. 408, 230–235.
MacLullich, A.M., Edmond, C.L., Ferguson, K.J., Wardlaw, J.M., Starr, J.M., Seckl, J.R., Deary, I.J., 2004. Size of the neocerebellar vermis is associated with cognition in healthy elderly men. Brain Cogn. 56, 344–348.
Maderwald, S., Thurling, M., Kuper, M., Theysohn, N., Muller, O., Beck, A., Aurich, V., Ladd, M.E., Timmann, D., 2012. Direct visualization of cerebellar nuclei in patients with focal cerebellar lesions and its application for lesion-symptom mapping. NeuroImage 63, 1421–1431.
Manjon, J.V., Coupe, P., Marti-Bonmati, L., Collins, D.L., Robles, M., 2010. Adaptive non-local means denoising of MR images with spatially varying noise levels. J. Magn. Reson. Imaging 31, 192–203.
Maschke, M., Weber, J., Dimitrova, A., Bonnet, U., Bohrenkamper, J., Sturm, S., Kindsvater, K., Muller, B.W., Gastpar, M., Diener, H.C., Forsting, M., Timmann, D., 2004. Age-related changes of the dentate nuclei in normal adults as revealed by 3D fast low angle shot (FLASH) echo sequence magnetic resonance imaging. J. Neurol. 251, 740–746.
Mathis, C., Collin, L., Borrelli, E., 2003. Oligodendrocyte ablation impairs cerebellum development. Development 130, 4709–4718.
Moller, H.E., Bossoni, L., Connor, J.R., Crichton, R.R., Does, M.D., Ward, R.J., Zecca, L., Zucca, F.A., Ronen, I., 2019. Iron, myelin, and the brain: neuroimaging meets neurobiology. Trends Neurosci. 42, 384–401.
Park, D.C., Reuter-Lorenz, P., 2009. The adaptive brain: aging and neurocognitive scaffolding. Annu. Rev. Psychol. 60, 173–196.
Paul, R., Grieve, S.M., Chaudary, B., Gordon, N., Lawrence, J., Cooper, N., Clark, C.R., Kukla, M., Mulligan, R., Gordon, E., 2009. Relative contributions of the cerebellar vermis and prefrontal lobe volumes on cognitive function across the adult lifespan. Neurobiol. Aging 30, 457–465.
Persson, N., Wu, J., Zhang, Q., Liu, T., Shen, J., Bao, R., Ni, M., Liu, T., Wang, Y., Spincemaille, P., 2015. Age and sex related differences in subcortical brain iron concentrations among healthy adults. NeuroImage 122, 385–398.
Peterson, E.T., Kwon, D., Luna, B., Larsen, B., Prouty, D., De Bellis, M.D., Voyvodic, J., Liu, C., Li, W., Pohl, K.M., Sullivan, E.V., Pfefferbaum, A., 2019. Distribution of brain iron accrual in adolescence: evidence from cross-sectional and longitudinal analysis. Hum. Brain Mapp. 40, 1480–1495.
Ramos, P., Santos, A., Pinto, N.R., Mendes, R., Magalhaes, T., Almeida, A., 2014. Iron levels in the human brain: a post-mortem study of anatomical region differences and age-related changes. J. Trace Elem. Med. Biol. 28, 13–17.
Raz, N., Gunning-Dixon, F., Head, D., Williamson, A., Acker, J.D., 2001. Age and sex differences in the cerebellum and the ventral pons: a prospective MR study of healthy adults. AJNR Am. J. Neuroradiol. 22, 1161–1167.
Reetz, K., Costa, A.S., Mirzazade, S., Lehmann, A., Juzek, A., Rakowicz, M., Boguslawska, R., Schols, L., Linnemann, C., Mariotti, C., Grisoli, M., Durr, A., van de Warrenburg, B.P., Timmann, D., Pandolfo, M., Bauer, P., Jacobi, H., Hauser, T.K., Klockgether, T., Schulz, J.B.axia Study Group, I., 2013. Genotype-specific patterns of atrophy progression are more sensitive than clinical decline in SCA1, SCA3 and SCA6. Brain 136, 905–917.

Reichenbach, J.R., Haacke, E.M., 2001. High-resolution BOLD venographic imaging: a window into brain function. NMR Biomed. 14, 453–467.
Reuter, M., Schmansky, N.J., Rosas, H.D., Fischl, B., 2012. Within-subject template estimation for unbiased longitudinal image analysis. NeuroImage 61, 1402–1418.
Roemer, P.B., Edelstein, W.A., Hayes, C.E., Souza, S.P., Mueller, O.M., 1990. The NMR phased array. Magn. Reson. Med. 16, 192–225.
Sanfilipo, M.P., Benedict, R.H., Zivadinov, R., Bakshi, R., 2004. Correction for intracranial volume in analysis of whole brain atrophy in multiple sclerosis: the proportion vs. residual method. NeuroImage 22, 1732–1743.
Sasaki, H., Kojima, H., Yabe, I., Tashiro, K., Hamada, T., Sawa, H., Hiraga, H., Nagashima, K., 1998. Neuropathological and molecular studies of spinocerebellar ataxia type 6 (SCA6). Acta Neuropathol. 95, 199–204.
Schäfer, A., Wharton, S., Gowland, P., Bowtell, R., 2009. Using magnetic field simulation to study susceptibility-related phase contrast in gradient echo MRI. NeuroImage 48, 126–137.
Schmitz-Hubsch, T., Coudert, M., Bauer, P., Giunti, P., Globas, C., Baliko, L., Filla, A., Mariotti, C., Rakowicz, M., Charles, P., Ribai, P., Szymanski, S., Infante, J., van de Warrenburg, B.P., Durr, A., Timmann, D., Boesch, S., Fancellu, R., Rola, R., Depondt, C., Schols, L., Zdienicka, E., Kang, J.S., Dohlinger, S., Kremer, B., Stephenson, D.A., Melegh, B., Pandolfo, M., di Donato, S., du Montcel, S.T., Klockgether, T., 2008a. Spinocerebellar ataxia types 1, 2, 3, and 6: disease severity and nonataxia symptoms. Neurology 71, 982–989.
Schmitz-Hubsch, T., du Montcel, S.T., Baliko, L., Berciano, J., Boesch, S., Depondt, C., Giunti, P., Globas, C., Infante, J., Kang, J.S., Kremer, B., Mariotti, C., Melegh, B., Pandolfo, M., Rakowicz, M., Ribai, P., Rola, R., Schols, L., Szymanski, S., van de Warrenburg, B.P., Durr, A., Klockgether, T., Fancellu, R., 2006. Scale for the assessment and rating of ataxia: development of a new clinical scale. Neurology 66, 1717–1720.
Schmitz-Hubsch, T., Giunti, P., Stephenson, D.A., Globas, C., Baliko, L., Sacca, F., Mariotti, C., Rakowicz, M., Szymanski, S., Infante, J., van de Warrenburg, B.P., Timmann, D., Fancellu, R., Rola, R., Depondt, C., Schols, L., Zdzienicka, E., Kang, J.S., Dohlinger, S., Kremer, B., Melegh, B., Filla, A., Klockgether, T., 2008b. SCA Functional Index: a useful compound performance measure for spinocerebellar ataxia. Neurology 71, 486–492.
Schöls, L., Bauer, P., Schmidt, T., Schulte, T., Riess, O., 2004. Autosomal dominant cerebellar ataxias: clinical features, genetics, and pathogenesis. Lancet Neurol. 3, 291–304.
Schöls, L., Kruger, R., Amoiridis, G., Przuntek, H., Epplen, J.T., Riess, O., 1998. Spinocerebellar ataxia type 6: genotype and phenotype in German kindreds. J. Neurol. Neurosurg. Psychiatry 64, 67–73.
Schulz, J.B., Borkert, J., Wolf, S., Schmitz-Hubsch, T., Rakowicz, M., Mariotti, C., Schols, L., Timmann, D., van de Warrenburg, B., Durr, A., Pandolfo, M., Kang, J.S., Mandly, A.G., Nagele, T., Grisoli, M., Boguslawska, R., Bauer, P., Klockgether, T., Hauser, T.K., 2010. Visualization, quantification and correlation of brain atrophy with clinical symptoms in spinocerebellar ataxia types 1, 3 and 6. NeuroImage 49, 158–168.
Schweser, F., Hagemeier, J., Dwyer, M.G., Bergsland, N., Hametner, S., Weinstock-Guttman, B., Zivadinov, R., 2021. Decreasing brain iron in multiple sclerosis: the difference between concentration and content in iron MRI. Hum. Brain Mapp. 42, 1463–1474.
Seidler, R.D., Bernard, J.A., Burutolu, T.B., Fling, B.W., Gordon, M.T., Gwin, J.T., Kwak, Y., Lipps, D.B., 2010. Motor control and aging: links to age-related brain structural, functional, and biochemical effects. Neurosci. Biobehav. Rev. 34, 721–733.
Spence, H., McNeil, C.J., Waiter, G.D., 2020. The impact of brain iron accumulation on cognition: a systematic review. PLoS One 15, e0240697.
Stefanescu, M.R., Dohnalek, M., Maderwald, S., Thurling, M., Minnerop, M., Beck, A., Schlamann, M., Diedrichsen, J., Ladd, M.E., Timmann, D., 2015. Structural and functional MRI abnormalities of cerebellar cortex and nuclei in SCA3, SCA6 and Friedreich's ataxia. Brain 138, 1182–1197.
Stilling, B., 1878. Neue Untersuchungen über Den Bau des Kleinen Gehirns des Menschen. Theodor Kay, Kassel.
Sugiyama, A., Sato, N., Kimura, Y., Fujii, H., Maikusa, N., Shigemoto, Y., Suzuki, F., Morimoto, E., Koide, K., Takahashi, Y., Matsuda, H., Kuwabara, S., 2019. Quantifying iron deposition in the cerebellar subtype of multiple system atrophy and spinocerebellar ataxia type 6 by quantitative susceptibility mapping. J. Neurol. Sci. 407, 116525.
Sullivan, E.V., Pfefferbaum, A., 2006. Diffusion tensor imaging and aging. Neurosci. Biobehav. Rev. 30, 749–761.
Sultan, F., Konig, T., Mock, M., Thier, P., 2002. Quantitative organization of neurotransmitters in the deep cerebellar nuclei of the Lurcher mutant. J. Comput. Neurol. 452, 311–323.
Tellmann, S., Bludau, S., Eickhoff, S., Mohlberg, H., Minnerop, M., Amunts, K., 2015. Cytoarchitectonic mapping of the human brain cerebellar nuclei in stereotaxic space and delineation of their co-activation patterns. Front. Neuroanat. 9, 54. doi:10.3389/fnana.2015.00054.
Thurling, M., Hautzel, H., Kuper, M., Stefanescu, M.R., Maderwald, S., Ladd, M.E., Timmann, D., 2012. Involvement of the cerebellar cortex and nuclei in verbal and visuospatial working memory: a 7 T fMRI study. NeuroImage 62, 1537–1550.
Torvik, A., Torp, S., Lindboe, C.F., 1986. Atrophy of the cerebellar vermis in ageing. A morphometric and histologic study. J. Neurol. Sci. 76, 283–294.
Trewartha, K.M., Garcia, A., Wolpert, D.M., Flanagan, J.R., 2014. Fast but fleeting: adaptive motor learning processes associated with aging and cognitive decline. J. Neurosci. 34, 13411–13421.
Triarhou, L.C., Norton, J., Ghetti, B., 1987. Anterograde transsynaptic degeneration in the deep cerebellar nuclei of Purkinje cell degeneration (pcd) mutant mice. Exp. Brain Res. 66, 577–588.
Voevodskaya, O., Simmons, A., Nordenskjold, R., Kullberg, J., Ahlstrom, H., Lind, L., Wahlund, L.O., Larsson, E.M., Westman, E.Alzheimer's Disease Neuroimaging, I., 2014. The effects of intracranial volume adjustment approaches on multiple regional MRI volumes in healthy aging and Alzheimer's disease. Front. Aging Neurosci. 6, 264.
Voogd, J., Ruigrok, T.J.H., Paxinos, J.K.M., 2012. Chapter 15 - cerebellum and precerebellar nuclei. In: The Human Nervous System. Academic Press, San Diego, pp. 471–545.
Wang, X., Wang, H., Xia, Y., Jiang, H., Shen, L., Wang, S., Shen, R., Huang, L., Wang, J., Xu, Q., Li, X., Luo, X., Tang, B., 2010. A neuropathological study at autopsy of early onset spinocerebellar ataxia 6. J. Clin. Neurosci. 17, 751–755.
Ward, P.G.D., Harding, I.H., Close, T.G., Corben, L.A., Delatycki, M.B., Storey, E., Georgiou-Karistianis, N., Egan, G.F., 2019. Longitudinal evaluation of iron concentration and atrophy in the dentate nuclei in friedreich ataxia. Mov. Disord. 34, 335–343.
Yang, Q., Hashizume, Y., Yoshida, M., Wang, Y., Goto, Y., Mitsuma, N., Ishikawa, K., Mizusawa, H., 2000. Morphological Purkinje cell changes in spinocerebellar ataxia type 6. Acta Neuropathol. 100, 371–376.
Yang, Z., Ye, C., Bogovic, J.A., Carass, A., Jedynak, B.M., Ying, S.H., Prince, J.L., 2016. Automated cerebellar lobule segmentation with application to cerebellar structural analysis in cerebellar disease. NeuroImage 127, 435–444.
Zecca, L., Youdim, M.B., Riederer, P., Connor, J.R., Crichton, R.R., 2004. Iron, brain ageing and neurodegenerative disorders. Nat. Rev. Neurosci. 5, 863–873.
Zheng, W., Nichol, H., Liu, S., Cheng, Y.C., Haacke, E.M., 2013. Measuring iron in the brain using quantitative susceptibility mapping and X-ray fluorescence imaging. NeuroImage 78, 68–74.